NASA Technical Memorandum 4676

Direct Adaptive Performance Optimization of Subsonic Transports: A Periodic Perturbation Technique

Martín España and Glenn Gilyard

March 1995

Direct Adaptive Performance Optimization of Subsonic Transports: A Periodic Perturbation Technique

Martín España
National Research Council
NASA Dryden Research Associate

Glenn Gilyard
NASA Dryden Flight Research Center
Edwards, California

Technical Memorandum 4676 March 1995

TABLE OF CONTENTS

ABSTRACT 1

NOMENCLATURE 1

INTRODUCTION 2

AIRCRAFT PERFORMANCE OPTIMIZATION 4
- Control Effectors 5
- Optimization Strategies 5
- Aircraft Model 6

PERIODIC PERTURBATION EXTREMA-SEARCHING TECHNIQUE 6
- Working Principle 6
- Control Law Structure: Analysis and Design 8

SINGLE-SURFACE VELOCITY MAXIMIZATION MODE 9
- Design Approach With Ideal Altitude-Hold Assumption 9
- Effects of Constraint Violation 12
- Adaptive Constraints Control: An Adaptive Noise-Cancelling Approach 13
- Results of Simulated Experiment 15

SINGLE-SURFACE FUEL-FLOW MINIMIZATION MODE 21
- Results of Simulated Experiment 23

MULTISURFACE OPTIMIZATION 23
- Velocity Optimization Mode: Results of Simulation Experiment 26
- Fuel-Flow Optimization Mode: Results of Simulation Experiment 29

CONCLUDING REMARKS 32

REFERENCES 34

APPENDIX A
- Sample Calculation of an Envelope Equivalent Transfer Function 35

APPENDIX B
- Optimization Offset Caused by Constraints Violations 36

APPENDIX C
- Adaptive Rejection of a Sinusoidal Disturbance 37

Abstract

Aircraft performance can be optimized at the flight condition by using available redundancy among actuators. Effective use of this potential allows improved performance beyond limits imposed by design compromises. Optimization based on nominal models does not result in the best performance of the actual aircraft at the actual flight condition. An adaptive algorithm for optimizing performance parameters, such as speed or fuel flow, in flight based exclusively on flight data is proposed. The algorithm is inherently insensitive to model inaccuracies and measurement noise and biases and can optimize several decision variables at the same time. An adaptive constraint controller integrated into the algorithm regulates the optimization constraints, such as altitude or speed, without requiring any prior knowledge of the autopilot design. The algorithm has a modular structure which allows easy incorporation (or removal) of optimization constraints or decision variables to the optimization problem. An important part of the contribution is the development of analytical tools enabling convergence analysis of the algorithm and the establishment of simple design rules. The fuel-flow minimization and velocity maximization modes of the algorithm are demonstrated on the NASA Dryden B-720 nonlinear flight simulator for the single- and multi-effector optimization cases.

Nomenclature

A	excitation amplitude, deg
ACC	adaptive constraints controller
C_D	drag coefficient
C_{D_u}	C_D sensitivity with respect to Mach number
C_{D_δ}	C_D sensitivity with respect to a generic decision variable
D	total drag, lb
E_p	potential energy
FC	flight condition (weight, center of gravity, altitude, winds, true airspeed)
G	transfer function gain
$G(s)$	transfer function
h	altitude, ft
J	optimized function
K	optimizer adaptation gain
L	lift, lb
m	mass of the aircraft, slugs
M	pitch moment, lb · ft
MAW	mission adaptive wing (F-111 program)
PI	performance index
PLA	power-lever angle, deg
PSC	performance-seeking control
$\bar{q}$	dynamic pressure $(1/2\rho V^2)$
R_ψ	ψ–rotation matrix

s	Laplace variable
$s(t)$	excitation signal
S	wing surface area (2433 ft^2)
T	thrust, lb
T_o	period of excitation signal, sec
T_{req}	thrust required, lb
u	control signal
U,M,N,P,Q	adaptive magnitudes of adaptive constraints controller
V	true airspeed, ft/sec
α	angle of attack, deg
β,τ	parameters of envelope equivalent system
Γ	curvature of optimized function J or performance index
γ	flightpath angle
δ_{ail}	aileron deflection, deg
δ_c	decision variable
δ_{el}	elevator deflection, deg
δ_{fl}	flap deflection, deg
δ_s	probing signal
δ_{surf}	generic surface deflection
$\delta(t)$	total input on decision variable
δ_o	initial value of decision variable
$\eta(t)$	trigonometric vector
μ	adaptation gain of adaptive constraints controller
ρ	air density, slug/ft^3
φ	phase angle, rad
ω_o	perturbation signal frequency, rad/sec

Introduction

Increasing competition among airline manufacturers and operators worldwide has spawned a recent all-out effort to reduce direct operating costs. Because an airline's net profit is the difference between two large numbers (revenues and costs) measured in percentage of the costs, a small reduction in direct costs can have considerable leverage in an industry with a profit margin of about 5 percent (ref. 1). After ownership costs (approximately 50 percent of direct operating costs), the second major driver of costs is fuel consumption, which accounts for approximately 18 percent (ref. 1). The effect of aircraft performance on an operator's profitability can be crucial because production costs are not usually under the operator's control. Improved performance can result in less required thrust and can benefit engine wear. This improvement can increase engine life and further reduce maintenance and direct operating costs.

NASA conducted research in the late 1970's and 1980's that aimed toward improving aircraft performance. This effort was part of the aircraft energy efficiency and advanced fighter technology integration programs. (Ref. 2 surveyed past attempts to apply active controls to improve aircraft perform- ance.) The F-111 mission adaptive wing (MAW) program (ref. 3) showed the potential for applying the variable wing camber concept to transport aircraft. Standard wing and wing configuration point designs, by necessity, represent the result of major compromises among numerous design considerations and flight conditions. By adapting the wing configuration to the particularities of the flight, variable wing cambering allows those design compromises to be overcome. The MAW program clearly demonstrated the effects of this technology on performance improvements. Two modes of the F-111 MAW are applicable to transport aircraft: the cruise camber control mode, which was designed for real-time adaptive optimization with drag reduction, and the maneuver camber control mode, designed to maximize lift-to-drag ratio (*L/D*).

Recent extensive wind-tunnel testing and flight experiments with wide-body transports, performed by the German company Messerschmitt-Bolkov-Blohm (now Deutsche Aerospace, a member of the Airbus Consortium), show that continuous camber variations can improve the efficiency of the most advanced wings, even at their best design points: a clear consequence of transcending the point design compromises (ref. 4). Besides drag improvements (potentially a 3- to 9-percent increase in *L/D* is reported in ref. 4), camber control may also improve other aspects of the aircraft design. For example, an increase of the maximum lift coefficient for the wing buffet onset (a 12-percent increase has been reported in refs. 4 and 5) or root bending moments alleviation is possible (ref. 6). The same team showed that coordinated deflections of flaps, ailerons, elevators, stabilator, and (possibly) leading-edge devices can induce variable wing cambering without the penalty of a new wing box design or a significant weight increase (refs. 4, 5, and 6). The team has not yet reported on any in-flight adaptive optimization scheme for performance improvement. Only prescheduled camber repositioning has been considered.

The performance-seeking control (PSC) program is NASA Dryden Flight Research Center's most recent attempt to develop an in-flight performance optimization algorithm. PSC was developed for optimizing the propulsion system of the F-15 highly integrated digital electronic control (HIDEC) research aircraft in quasi-steady state. PSC encompasses the following optimization modes: (a) minimum fuel flow at constant thrust, (b) minimum turbine temperature at constant thrust, and (c) maximum thrust. Both subsonic and supersonic flight testing of the PSC algorithm has been concluded and reported by NASA Dryden (ref. 7). The PSC program demonstrates that performance can be accrued beyond the design point with in-flight optimization; however, as an open-loop optimization scheme (no direct measure of a performance index (PI) is used), it relies heavily on *a priori* models. Model errors may, therefore, influence considerably the optimization process, especially when only low-level performance improvements are expected. Measurement biases also impact the estimation of the current engine parametrization used subsequently to feed the optimization model in PSC. (Refs. 8 and 9 analyzed the influence of measurement biases over the estimation process of PSC.) To accommodate the above problems, reference 7 suggested a closed-loop technique based on a direct measurement of a PI.

Such a technique should take into account the particularities of actual flight conditions without being sensitive to model changes or model uncertainties. The MAW program pioneered that type of approach for its CCC mode using a trial-and-error algorithm, which works for large drag changes (i.e., 5 to 10 percent) but fails for low-level drag changes (i.e., 1 to 2 percent). Thus, both the PSC and MAW approaches for in-flight optimization are unsuitable for the low-level drag improvement expected in transport aircraft, albeit for different reasons. Accordingly, the development of a robust and efficient algorithm for in-flight aircraft performance optimization is in order.

This paper proposes a perturbational technique (ref. 10) for the adaptive optimization of an aircraft's performance through excess thrust improvements. The algorithm, called adaptive performance optimization, estimates, online, the correlations between periodic perturbations introduced on the decision variables and their effects on a measured PI. The estimated correlations are then used to decide average changes on the decision variables that (locally) improve the PI. The optimization technique can be viewed as belonging to the gradient-type family, but, instead of signal differentiation, it uses averaging and signal integration. This characteristic gives the algorithm its strong robustness with respect to signal measurements' noise and biases.

For the application at hand, the optimization is performed using the available redundancy among surface effectors. The measured performance index (PI) includes the contributions coming, simultaneously, from the airframe and the engines to the overall performance changes.

Sensors and instrumentation are, undoubtedly, important elements in any flight performance optimization research program. The issues, however, related to those elements are beyond the scope of this report, which focuses on the methodological aspects of the inflight optimization technique.

Following a general discussion of the aircraft performance optimization problem, the working principle of the proposed optimization technique is described. Then, a design procedure is suggested for the speed-maximization mode at constant altitude and power lever angle (PLA). The deflections of the surfaces involved (i.e., symmetric outboard ailerons and elevator) are linked by the constant altitude constraint. This link between the surfaces transforms the problem into a single decision variable (or single-surface) optimization. First, the control of the optimization constraint is left to the autopilot, which attempts to keep the net pitch moment equal to zero and the altitude constant. Up to this point, the paper closely follows that of España and Gilyard (ref. 11). Discussed here for the first time are some limitations of that approach when fast perturbation signals are used. It is shown that, if no provisions are taken, with a practical (nonideal) autopilot, the perturbations signals may induce oscillations on the constraints that steer the algorithm away from the optimum values for the decision variables. A solution to this problem, based on an adaptive oscillation canceller technique, is then proposed and tested in simulation.

A fuel-flow minimization mode is next considered for constant altitude and speed. It is shown that a natural extension of the algorithm for the speed-maximization mode at constant altitude is able to take into account the extra constraint of the fuel-flow minimization mode. The algorithm also compensates for the effects of nonideal altitude- and velocity-hold functions of the autopilot.

Both modes (velocity maximization and fuel-flow minimization) are then tested in simulation using more than one degree of freedom by optimizing simultaneously with respect to outboard ailerons and outboard flaps (multisurface optimization) while keeping the elevator as the compensating effector for pitch and altitude control. The testbed used was the B-720 nonlinear flight simulator at NASA Dryden's Simulation Laboratory. The simulations assume full precision of all variables used in the feedback control laws.

Aircraft Performance Optimization

Most aircraft have a significant redundant control effector capability (i.e., more than one means of trimming out the forces and moments to obtain a steady-state flight condition). The challenging task of taking advantage of such capability for an aircraft adaptive in-flight performance optimization is the subject of this report.

Control Effectors

Drag minimization potential exists for the entire spectrum of subsonic transport aircraft. Aircraft manufacturers recognize the potential for performance improvements based on available control effectors and have implemented some fixed-point reriggings based on flight test results.

Figure 1 illustrates the controls or variables that show potential for optimizing the performance of current-generation aircraft. These variables include elevator, horizontal stabilizer, outboard aileron, inboard aileron, flaps, slats, rudder, and center of gravity. Spoilers are not an option for performance optimization, although spoilers may be a viable controller for drag modulation. Potential selected control variable tradeoffs are possible between:

- Symmetric aileron or flap (leading edge and trailing edge), or both, and horizontal stabilizer or elevator
- Inboard and outboard symmetric aileron or flap, or both
- Elevator and horizontal stabilizer
- Inboard and outboard elevator
- Center of gravity and horizontal stabilizer
- Rudder and differential thrust
- Sideslip and rudder deflection

Optimization Strategies

In the following analysis, two optimization modes that take advantage of an increase in excess thrust* at constant altitude cruise flight are considered: velocity maximization with constant PLA and fuel-flow minimization at constant speed. In the velocity-maximization mode, an excess thrust increase is sensed as an instantaneous acceleration increase. In this mode, the acceleration, aircraft speed, or both, is used as a PI (subject to the altitude constraint). When altitude and velocity are both constrained, excess thrust changes are reflected in thrust and fuel-flow changes. Constant velocity and altitude constraints are achieved by the autopilot through an inner control loop with respect to the optimizing

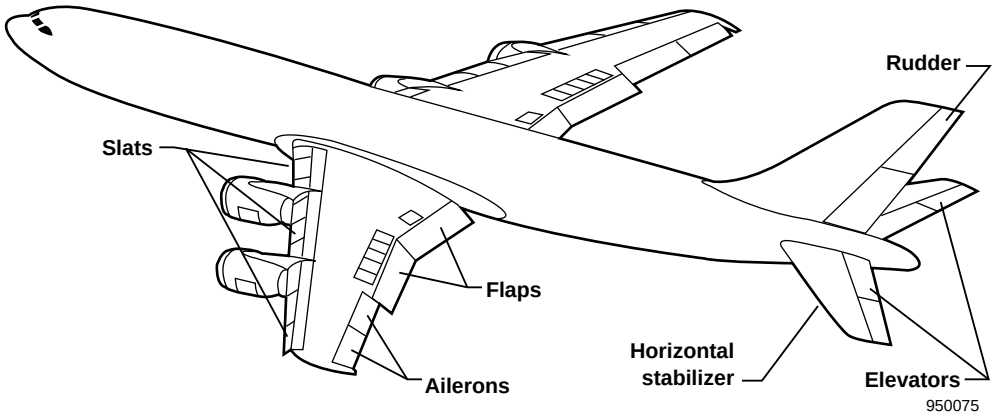

Figure 1. Typical subsonic transport control effectors.

*In practice, for subsonic aircraft at cruise conditions, the main contribution to performance increase comes from airframe drag reduction. However (technically, at least), the magnitude being optimized is the excess thrust defined as thrust minus drag. This allows for a more general algorithm perspective.

control law. When only the altitude is held, the autopilot commands the elevator exclusively. When both altitude and velocity are held, the autopilot also sets the PLA.

Aircraft Model

The simulation results were obtained with a simulated B-720 at the nominal cruise flight condition: altitude 30,000 ft, Mach number 0.80, standard atmospheric day, total weight 200,000 lb. The original model was designed for low-speed flight conditions; drag characteristics of the control surfaces were not modeled or even available. Some modifications were required to conduct performance optimization algorithm design–evaluation at cruise flight conditions. Adding quadratic drag effects as a function of aileron and flap deflection (i.e., C_{D_δ}) incorporated realistic drag characteristics into the model. In addition, a term representing drag increases with Mach, C_{D_u}, was included. Fuel burn and aeroelastic effects were not considered. All simulation control laws used the full precision and accuracy of the variables for feedback control. All variables required for feedback were assumed to be available. No gust, turbulence, or noise effects were simulated.

Periodic Perturbation Extrema-Searching Technique

Adaptive optimization techniques with periodic perturbation and direct feedback of a measurable PI allow for direct optimization of the PI without requiring a model (refs. 10 and 12).

Working Principle

The technique, first proposed in reference 12, consists of using sinusoidal probing signals superimposed on each of the decision variables of the optimization problem. A separate probing signal frequency is assigned to each decision variable. Online estimation of the correlations between the sinusoidal perturbations and PI are used to approximate the components of the local gradient of the PI with respect to the decision variables. The gradient thus estimated is then used as the search direction in the decision variable space to improve the PI value. The basic principle of the algorithm is better described for a quadratic single-input PI, here indicated by J.

For positive constants K and Γ, consider the unconstrained optimization of the function $J(\cdot)$ of a single decision variable δ (Γ will be referred as to the *curvature* of J):

$$J(\delta) = J(\delta^*) + \frac{1}{2}\Gamma(\delta - \delta^*)^2 \tag{1}$$

The optimization algorithm is given by the equations (ref. 10):

$$\delta(t) = \delta_c(t) + \delta_s(t); \;\; \delta_s(t) = A\sin(\omega_o t) \tag{2a}$$

$$\dot{\delta}_c = -KJ(\delta(t))A\sin(\omega_o t - \varphi); \;\; \delta_c(0) = \delta_o \tag{2b}$$

where δ_c is the decision variable with initial value δ_o and optimal value δ^*. The probing signal δ_s is superimposed on δ_c to give the total input $\delta(t)$. The phase angle φ is a design parameter whose interest will become clear later. The differential equation (2b) links, in a way that is discussed later, the search speed with the input-output correlation of function J.

Given its nonlinear character, an exact analytical description of equations (1) and (2) is a complicated task. An approximated analysis is based on the assumption that $\delta_c(t)$ changes much more slowly than the sinusoidal probing signal δ_s and $J(t)$. This slow variation is ensured by choosing a sufficiently small integration gain K, also a design parameter. The analysis technique (see, for example, ref. 13, chap. 6)

consists of substituting the right-hand side of equation (2b) by its time average over a receding horizon of time with length equal to the period $T_o = 2\pi/\omega_o$.

For an arbitrary function $f(t)$, the T_o-averaged function $\bar{f}(t)$ is defined as

$$\bar{f}(t) := avg\{f(t)\} := \frac{1}{T_o}\int_{t-T_o}^{t} f(\tau)d\tau \tag{3}$$

where τ is the integration variable. The following first-order approximation around $\delta_c(t)$ of expression (1) is also used:

$$J(A\sin(\omega_o t) + \delta_c(t)) \cong J(\delta_c(t)) + \Gamma(\delta_c(t) - \delta^*)A\sin(\omega_o t) \tag{4}$$

With approximation (4) and definition (3), the averaged right-hand side of equation (2b) is calculated as

$$\begin{aligned} &K\Gamma(\bar{\delta}_c(t) - \delta^*)A^2 avg\{\sin(\omega_o t)\sin(\omega_o t - \varphi)\} \\ &= \frac{1}{2}K\Gamma(\bar{\delta}_c(t) - \delta^*)A^2 avg\{\cos(\varphi) - \cos(2\omega_o t - \varphi)\} \end{aligned} \tag{5}$$

where, by assuming that $\delta_c(t)$ remains almost constant during a time interval T_o, $\delta_c(t)$ is approximated by the T_o-averaged function $\bar{\delta}_c(t)$.

From equation (5), the solutions of the nonlinear and time-varying differential equation (2b) are approximated by those resulting from the averaged linear and time-invariant differential equation (it can be easily shown using definition (3) that $\dot{\bar{\delta}}_c = \bar{\dot{\delta}}_c$):

$$\dot{\bar{\delta}}_c \cong -\frac{1}{2}K\Gamma(\bar{\delta}_c - \delta^*)A^2\cos(\varphi) \tag{6}$$

Whenever $\varphi \in (-\pi/2, \pi/2)$, $\bar{\delta}_c$ converges exponentially to the optimum value δ^* with time constant $2/[KA^2\,\Gamma\cos(\varphi)]$. Two important properties can be derived from the above analysis:

P1: *In the average,* δ_c *tends exponentially toward its optimal value* δ^* *for wide ranges of* φ, K, *and* Γ.

P2: *In the average, biases on the measurements do not affect this result because, from equations (3) through (5), their averaged effect on equation (6) is zero.*

To obtain the next result, we now assume that, for a large enough time t', (practical) convergence has already been achieved, and thus, if n is an integer such that $t = nT_o > t'$, then $\bar{\delta}_c(t) = \delta_c^\infty = \delta_c^*$. From equation (2b), we now can write

$$\bar{\delta}_c(t) = \delta_c^* \cong \delta_c(t) = \delta_c^* - K\int_{t'}^{t} J(\tau)A\sin(\omega_o\tau - \varphi)d\tau \tag{7}$$

Thus, the following necessary condition for convergence follows:

$$\mathrm{corr}\left\{J, e^{-j\varphi}\,\delta_s\right\} := \lim_{t\to\infty}\frac{1}{t-t'}\int_{f}^{t} J(\tau)A\sin(\omega_o\,\tau - \varphi)d\tau = 0 \tag{8}$$

Equation (8) shows that the algorithm attempts to adjust the value of δ_c so that the correlation of the PI and the excitation signals is zero. This correlation interpretation of the algorithm, and the fact that sinusoidal signals of different frequencies have zero correlation, explain another important property of the algorithm; namely,

> P3: *The effects that an additive measurement noise on PI have on the average of* δ_c *are negligible unless the noise power spectrum is concentrated around the excitation frequency* ω_o.

Control Law Structure: Analysis and Design

Figure 2 shows a block diagram of a practical extremum-searching system with a single-decision variable (for the application addressed in this paper the decision variable δ will be a control surface deflection). The plant's PI measurement process is represented by the nonlinear static characteristic $J(\cdot)$ in series with a linear filter $G_p(s)$ representing possible sensor dynamics. The transfer functions G_f and G_a are, respectively, a signal-shaping filter used to eliminate undesired frequency components at either side of ω_o, and a low-pass filter. All transfer functions are assumed to have unitary gains. The tandem (M, G_a) in figure 2 acts as a demodulator, eliminating most of the ω_o-harmonics remaining in the feedback loop (mainly the $2\omega_o$ term; see eq. (5)). As an exponentially weighted time average of the product π, the output of G_a (the convolution between the low-pass impulse response and π) is seen as an estimate of the current correlation between the inputs to the multiplier M. The cascaded block $G_fG_p(s)$ introduces a phase angle φ_o at the frequency ω_o.

For design and analysis purposes, only the information contained in the low-frequency components of the signals in the circuit is of interest. For that reason, following the guidelines of reference 10, chapter 9, the system in figure 2 is transformed into an equivalent low-pass network. Figure 3 shows the corresponding equivalent network for a quadratic J as in equation (1).

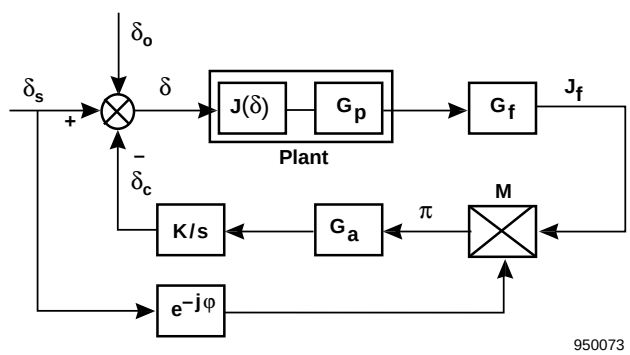

Figure 2. A single-dimensional extremum-searching algorithm.

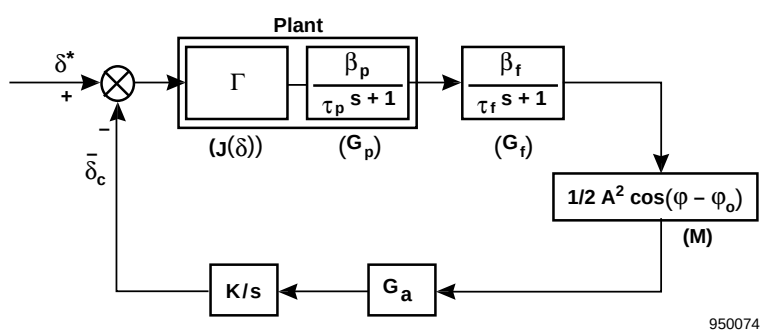

Figure 3. Envelope equivalent circuit.

Under each block of figure 3 is indicated, in parentheses, the originating block from figure 2. In the same figure, $\bar{\delta}_c$ represents the low-frequency component average of the feedback signal δ_c. The parameters of the equivalent system are calculated (see ref. 10 and the example in appendix A) as

$$\beta_p = |G_p(j\omega_o)|; \ \tau_p = -\left.\frac{\partial\varphi_p(\omega)}{\partial\omega}\right|_{\omega=\omega_o}$$
$$\beta_f = |G_f(j\omega_o)|; \ \tau_f = -\left.\frac{\partial\varphi_f(\omega)}{\partial\omega}\right|_{\omega=\omega_o} \tag{9}$$

where $|G(j\omega_o)|$ and $\varphi(\omega_o)$ indicate, respectively, the module and the phase angle of the transfer function G at $j\omega_o$. The equivalent network in figure 3 is used for the stability analysis and design purposes of the adaptive optimization algorithm. The designer has at his disposal the gain K, the phase compensation φ, the perturbation signal amplitude A, and the frequency ω_o. The transfer functions of the filters G_f and G_a can also be used to refine the design. For K sufficiently small (as we saw, a small K is also required for the validity of our analysis), $\tau_p > 0$, $\tau_f > 0$ (which is the case in practice), and φ selected such that $\varphi - \varphi_o \in (-\pi/2, \pi/2)$. The integrator on the feedback path ensures the exponential convergence of $\bar{\delta}_c$ to its optimal value δ^* under wide changes of the open loop gain (i.e., G, β_f, β_p etc.).** The convergence to the optimum is, thus, a robust property of the algorithm.

Single-Surface Velocity Maximization Mode

For the sake of clarity, we first consider the speed-maximization mode. The fuel-flow minimization mode, proposed later, is seen as a natural extension of the speed-maximization mode.

Design Approach With Ideal Altitude-Hold Assumption

This mode makes use of an altitude hold with the PLA kept at a constant position. From the three-degrees-of-freedom longitudinal flight equations of motion (ref. 14),

$$m\dot{V} = -D - mg \sin\gamma + T\cos\alpha \tag{10a}$$

$$mV\dot{\gamma} = L - mg\cos\gamma + T\sin\alpha \tag{10b}$$

$$I_{yy}\dot{q} = M \tag{10c}$$

$$\dot{h} = V\sin\gamma \tag{10d}$$

The wind component of the acceleration is given by

$$\dot{V} = \frac{1}{m}\left[T(\underline{\delta}, \mathrm{FC})\cos\alpha - \bar{q}(V, \rho)\, SC_D\,(\underline{\delta}, \mathrm{FC}) - mg\sin\gamma\right] \tag{11}$$

Flying conditions (FC) includes all the uncertainties and unmodeled effects of changing factors, such as weight, center-of-gravity position, winds/aircraft velocity, altitude, and aging engines and surfaces. The expression $T(\underline{\delta}, \mathrm{FC})$ corresponds to the unknown actual (as opposed to nominal) engine static characteristics relating thrust with the FC at constant PLA. The vector $\underline{\delta}$ in equation (11) is a generic vector of independent decision variables. The dependence of T on $\underline{\delta}$ emphasizes possible effects of the

**This can be concluded from the diagram of figure 3 using standard linear techniques (e.g., root locus).

surface configuration on the net engine thrust during the optimization (mainly because of airspeed changes in magnitude and direction). Two decision variables, the deflections of outboard ailerons (δ_{ail}) and outboard flaps (δ_{fl}), are considered in this report. This section considers only one independent surface deflection denoted generically as δ_{surf} ($\in \{\delta_{ail}, \delta_{fl}\}$) The other surface is assumed at its nominal deflection, typically $\delta = 0$. The elevator deflection δ_{el} is a dependent variable and, thus, does not explicitly appear in equation (11). The deflection δ_{el} is implicitly determined by δ_{surf} and the given level flight condition.

We designate as optimal the surface configuration that maximizes the excess thrust: $T - S\bar{q}C_D$. With the assumption of an ideal altitude hold, i.e., $\gamma = \dot{\gamma} = 0$, it is seen from equation (11) that the optimum corresponds to an extremum of $\dot{V}$. This latter variable can thus be used as the measurable PI for the optimization. In practice, the velocity V may be a better parameter than $\dot{V}$ in terms of available sensor resolution. For this purpose, España and Gilyard (ref. 11) suggested an algorithm modification that allows the use of V (instead of $\dot{V}$) as the measurable PI. That modification will not be considered in this report, whose focus is on more general methodological issues.

The optimal deflection δ^*_{surf} must satisfy the necessary condition for optimality:

$$\left.\frac{\partial \dot{V}}{\partial \delta_{surf}}\right|_{\delta^*_{surf}} = \frac{1}{m}\left[\frac{\partial}{\partial \delta_{surf}} T(\underline{\delta}, \mathrm{FC}) \cos\alpha - \bar{q}(V, \rho)\, S \frac{\partial}{\partial \delta_{surf}} C_D(\underline{\delta}, \mathrm{FC})\right]\Bigg|_{\delta^*_{surf}} = 0 \tag{12}$$

$$\dot{V}(\delta^*_{surf}) = 0$$

Figure 4 shows the autopilot and optimizer loops for a single surface optimization (δ_{surf}); h, $\dot{h}$, and h_D are, respectively, the altitude, its time-derivative, and the engaged (desired) altitude; $\delta_s = A \sin(\omega_o t)$ is the excitation or probing signal; δ^{ap}_{el} is the elevator command generated by the altitude hold (autopilot); δ_c is the surface command generated by the optimizer; δ_o is any initial estimate of the optimal deflection.

The frequency ω_o of the sinusoidal excitation δ_s, as well as its amplitude A, is chosen small enough that the dynamics of the aircraft in closed-loop operation with the autopilot can be neglected. Such a choice is required to ensure the validity, in practice, of the ideal autopilot assumption. For the design, the sensor dynamics (fig. 3) are also neglected by assuming $\beta_p = 1$ and $\tau_p = 0$.

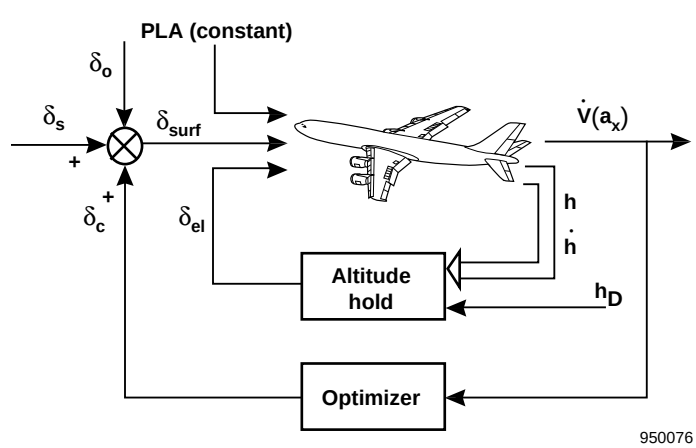

Figure 4. Autopilot and external optimizer loops.

The effects of configuration changes on the engine's net thrust are not taken into account for design and analysis purposes. The underlying approximation allows for a simplified design procedure as well as a deeper insight into the qualitative and quantitative aspects of the performance optimization algorithm. Nominal aero data are used to determine the trim-drag characteristic for the nominal flight conditions as a function of the independent surface δ_{surf} varying in its admissible range. (At each point of the characteristic, the dependent variable δ_{el} takes the value necessary to compensate for moment changes.)

The (nominal or measured) trim point characteristic relating δ_{surf} with C_D (trim drag coefficient) is fitted with a second-order polynomial from which the characteristic's average curvature Γ_{CD} is determined (eq. (1)). Now, from the incremental relationship,

$$\Delta\dot{V} = -\frac{S\Delta C_D\bar{q}}{m} \tag{13}$$

obtained from equation (11), the average curvature for the PI ($\dot{V}$ in this case) is determined as (eq. (1)): $\Gamma_{acc} = \bar{q}\,\Gamma_{CD}\,S/m$. Notice that, given the algorithm's convergent properties, discussed in the previous section, the above constants need only be known approximately. For simplicity, the mass is assumed constant in this paper (no fuel burn). In practice, the mass value used in equation (13) could be updated periodically with an estimate of the fuel consumed. As stated before, changes in the actual Γ_{acc} will only affect the convergence dynamics of the algorithm, not the final value.

To keep the design simple, G_f and G_a in figure 2 are chosen as the first-order transfer functions:

$$G_f = \frac{s}{s+\omega_h};\quad G_a = \frac{\omega_l}{s+\omega_l} \tag{14}$$

Given the roles of G_a and G_f, ω_o has to be simultaneously on the band pass of G_f and out of the band pass of G_a. For this purpose, the simple choice (admittedly, somewhat an arbitrary one) is adopted: $\omega_h = \omega_l = \omega_o/2$. The phase angle induced by G_f at ω_o can be shown to be $\varphi_f = 26.5°$. Because the dynamics of the aircraft have been neglected, we choose, in figures 2 and 3, $\varphi = \varphi_o = \varphi_f$. From equations (9), we then have

$$\begin{aligned} \beta_f &= \frac{\omega_o}{(\omega_o^2+\omega_h^2)^{1/2}} = 2/\sqrt{5} \\ \tau_f &= \frac{\omega_h}{(\omega_o^2+\omega_h^2)} = \frac{2}{5\omega_o} \end{aligned} \tag{15}$$

From equations (14) and (15), the open-loop transfer function poles of the equivalent system in figure 3 are 0, $\omega_o/2$, $5\omega_o/2$. After normalizing by ω_o, the open-loop transfer function results in

$$\frac{G/\omega_o^3}{s/\omega_o\,(s/\omega_o+1/2)\,(s/\omega_o+5/2)};\quad \bar{G} := \frac{G}{\omega_o^3} = \frac{A^2\sqrt{5}K}{4\omega_o}\left(\frac{\bar{q}S\Gamma_{CD}}{m}\right) \tag{16}$$

where G is the combined (nondimensional) gain of the blocks J, G_f, M, G_a, and K/s of figure 3 put in cascade. The normalized dynamics of the performance optimization algorithm are characterized by the closed-loop poles of the transfer function (16). Those poles can be conveniently placed by an appropriate choice of the normalized gain $\bar{G}$. The critical normalized gain for a deadbeat response can be shown to be $\bar{G}_c = 0.1408$, with a corresponding pair of coincident normalized dominant closed-

loop poles at –0.24 and a single normalized fast pole at –2.52. With the above choice of G, the normalized closed-loop response enters the 5-percent band around the final value at approximately 20 sec. As a consequence, the optimizer with excitation frequency ω_o is expected to reach the 5-percent band of the optimum at $20/\omega_o$ sec. The algorithm's gain K is calculated from equation (16) after appropriate constants substitutions. This completes the algorithm design. Equation (16) also gives a way to schedule K with the dynamic pressure $\bar{q}$ (281 lb/ft^2 for the nominal flight condition, i.e., altitude 30,000 ft, Mach number 0.8). Notice that for a given design criterion (a critical design criterion is chosen in this report), the adaptation gain, the corresponding closed-loop poles, and consequently, the convergence speed of the algorithm are all proportional to the excitation frequency ω_o.

Effects of Constraint Violation

To search for the optimal condition, the adaptive performance optimization algorithm uses estimated correlations between the PI and sinusoidal probing signals applied to the decision variables. For the velocity maximization mode with fixed throttle position, the horizontal acceleration (measurable PI) is a direct measure of the excess thrust only if the ideal altitude-hold assumption (namely, $\dot{h} = 0$ or $\gamma = \dot{\gamma} = 0$) is satisfied. In practice, however, the latter condition is satisfied only approximately, and the altitude's derivative features remnant oscillations of frequency ω_o. Those oscillations may have a determinant effect on the algorithm convergence properties. In fact, appendix B shows that the difference between the final value δ_{surf}^{∞} attained by the algorithm and the optimum δ_{surf}^{*} is approximated by

$$\delta_{surf}^{\infty} - \delta_{surf}^{*} \cong -\frac{2mg}{\Gamma_D A^2}\,\mathrm{corr}\{\dot{h}/V, \delta_s\} \tag{17a}$$

$$\cong -\frac{2}{\Gamma_D \bar{V}_\infty A^2}\,\mathrm{corr}\{\dot{E}_p, \delta_s\} \tag{17b}$$

where, by definition, $\Gamma_D := \bar{q}\,S\Gamma_{CD}$; corr{ . , . } indicates the temporal correlation between the signals inside the brackets; $\bar{V}_\infty$ is the average final velocity; and E_p is the aircraft's potential energy. The offset with respect to the optimum, indicated in equations (17), cannot be compensated for unless a detailed mathematical description of the aircraft is known beforehand. This is precisely what the optimization methodology intends to avoid. Given the low level of performance improvement expected and the direct influence of the total aircraft weight (mg in eq. (17a)), those deviations may be significant for large transport aircraft. Moreover, the offset may be magnified in multivariable optimization because a superposition of the effects of the individual loops could be expected in this case.

Equation (17b) gives an energy interpretation of the optimization offset. If the altitude is varying, an excess thrust change is not necessarily spent totally into a kinetic energy change but also into a potential energy rate-of-change that goes undetected by the measured PI ($\dot{V}$). Interestingly, changes in $\dot{E}_p$ induced by changes in environmental conditions (such as gusts, winds, and air density changes), un- correlated with respect to δ_s, will not produce, on the average, any optimization offset. This is inherent to the correlation approach used to estimate the gradient, given that only those changes correlated with δ_s are weighted by the online correlator.

We now denote by $G_\gamma(s)$ the transfer function between δ_s and the path angle γ when the altitude hold is in the loop. Recalling that $\delta_s(t) = A\sin(\omega_o t)$, equation (17a) is transformed into (appendix B)

$$\delta_{surf}^{\infty} - \delta_{surf}^{*} \cong \frac{2mg}{\Gamma_D\left(1/\left|G_\gamma(j\omega_o)\right|\right)}\cos\left(\varphi_\gamma(j\omega_o)\right) \tag{18}$$

where $|G_\gamma(j\omega_o)|$ is the module, and $\varphi_\gamma(j\omega_o)$ is the phase angle of $G_\gamma(s)$ at $j\omega_o$. The factor $1/|G_\gamma(j\omega_o)|$ is the disturbance rejection at ω_o provided by the altitude hold over the path angle. The altitude hold is typically designed so as to make $1/|G_\gamma(j\omega_o)|$ big at very low frequencies (integrator in the loop). For increasing frequencies, the autopilot rejection capability deteriorates, thus increasing the optimization offset. Consequently, because low excitation frequencies correspond to slow algorithm convergence (see comments following eq. (16)), the algorithm imposes a compromise between convergence speed and accuracy. The next section proposes a solution to this compromise.

Adaptive Constraints Control: An Adaptive Noise-Canceling Approach

To resolve the compromise just mentioned, the constraint control function of a practical autopilot may need to be enhanced. However, because the autopilot design requirements are specific to the type of aircraft and mission, a method that requires the redesigning of the autopilot to fit the needs of the optimizer is not desired in practice. The compromise is solved by using an adaptive constraint control technique that leaves the autopilot untouched and, even more interesting, does not require any *a priori* knowledge of the autopilot.

Adaptive noise-canceling techniques are particularly effective for eliminating undesired disturbances with known frequency spectra. The technique was pioneered for the discrete time case by Widrow and others (refs. 12 and 13). In appendix C, the continuous time version of the algorithm, suited for the application at hand, is derived using current adaptive theory tools.

In our problem, we seek to eliminate the ω_o-frequency oscillations present in $\dot{h}$ (or at least to decorrelate them with respect to the probing signal δ_s; see equations (17)). Synthesizing a sinusoidal elevator command signal δ_{el}^s with adequate phase and magnitude can compensate for the excitation signals introduced on the optimizing surface (the aileron in this case).

We assume, for the moment, that superposition can be invoked to decompose $\dot{h}$ in the following way (linearity assumption):

$$\dot{h} = \dot{h}_b + \dot{h}_s + \hat{\dot{h}}_s = \dot{h}_b + \dot{h}_s + G_{el}(j\omega_o)\delta_{el}^s \tag{19}$$

where $\dot{h}_s$ is the aircraft-autopilot $\dot{h}$-response to the probing signal δ_s applied to the ailerons' command; $\hat{\dot{h}}$ is the effect on $\dot{h}$ caused by the compensating signal δ_{el}^s; $\dot{h}_b$ is the basic $\dot{h}$ component not reflecting the effects of δ_s and δ_{el}^s; and $G_{el}(j\omega_o)$ is the transfer function between the elevator and $\dot{h}$. We now define $S,\eta \in \Re^2$ as

$$S^T := [X,Y],\ \eta^T(t) := [\cos(\omega_o t),\quad \sin(\omega_o t)] \tag{20}$$

With an adequate choice of the vector S, any sinusoidal signal $s(t)$ of known frequency ω_o can be written as

$$s(t) = X\cos(\omega_o t) + Y\sin(\omega_o t) = S^T\eta(t) \tag{21}$$

In particular, the (unknown) compensating elevator's signal command is expressed as

$$\delta_{el}^s(t) = \hat{U}^T\eta(t) \tag{22}$$

where $\hat{U}^T := [\hat{M}, \hat{N}]$ is the parameter vector, to be determined by the adaptive algorithm, such that $\dot{h} + \hat{h}_s \to 0$. Now, for $|G_{el}(j\omega_o)|$ and $\psi(j\omega_o)$, respectively, the magnitude and phase angle of the transfer function $G_{el}(j\omega_o)$, we can also express $\hat{\dot{h}}_s$ as

$$\begin{aligned} \hat{\dot{h}}_s(t) &= |G_{el}(j\omega_o)|(\hat{M}\cos(\omega_o t + \psi) + \hat{N}\sin(\omega_o t + \psi)) \\ &= |G_{el}(j\omega_o)|\hat{U}^T R_\psi \eta(t) \end{aligned} \tag{23}$$

where R_ψ indicates the ψ-rotation matrix. Following the results of appendix C for μ_e: $0 < \mu_e << 1$, $\hat{U}$ can be adapted with the algorithm:

$$\dot{\hat{U}} = -\mu_e \dot{h}\eta(t) \tag{24}$$

The transfer function G_{el} relates aerodynamic forces/moments (proportional to the elevator's deflection) with a mechanical speed. In consequence, as a simple mechanical argument shows, G_{el} has a dominant pole at the origin, implying a phase shift of approximately $-\pi/2$. Under these conditions, the use of the modified version

$$\dot{\hat{U}} = -\mu_e \dot{h} R_{\psi_o} \eta(t) \tag{25}$$

is recommended in appendix C, where the rotation matrix R_{ψ_o} is introduced into the algorithm to improve stability and convergence speed when an estimate ψ_o of ψ is available.

Summarizing, for $\psi_o = -\pi/2$, the adaptive velocity maximization algorithm with adaptive constraints controller (ACC) is given by the following set of equations ($\Delta_c(s)$ and $\Pi(s)$ denote, respectively, the Laplace transforms of $\delta_c(t)$ and $\pi(t)$):

$$\pi(t) = A\dot{V}\sin(\omega_o t - \varphi) \tag{26a}$$

$$\Delta_c(s) = \frac{KG_a(s)}{s}\Pi(s) \tag{26b}$$

$$\delta_{ail} = \delta_c + A\sin(\omega_o t) \tag{26c}$$

$$\delta_{el} = \delta_{el}^{ap} + \delta_{el}^{s} \tag{26d}$$

$$\dot{\hat{M}} = -\mu_e \dot{h}\cos(\omega_o t - \pi/2) = -\mu_e \dot{h}\sin(\omega_o t) \tag{26e}$$

$$\dot{\hat{N}} = -\mu_e \dot{h}\sin(\omega_o t - \pi/2) = \mu_e \dot{h}\cos(\omega_o t) \tag{26f}$$

$$\delta_{el}^{s}(t) = \hat{M}\cos(\omega_o t) + \hat{N}\sin(\omega_o t) \tag{26g}$$

Figure 5 depicts the resulting block diagram of ACC (adaptive disturbance rejection on the $\dot{h}$ signal). The changes in the interconnections for the diagram of figure C-2 of appendix C account for the $-\pi/2$ rotation required on $\eta(t)$.

Arguments similar to those leading to equation (8) allow us to interpret equations (26e) to (26g) as an adaptive mechanism to decorrelate the fundamental ω_o-harmonic in $\dot{h}$ with respect to $\delta_s(= A\sin(\omega_o t))$. From equation (17a), this is the necessary condition to suppress the bias in the optimization (higher harmonics of ω_o are decorrelated with the fundamental ω_o). Because convergence only requires decorrelation between (the fundamental harmonic of) $\dot{h}$ and δ_s (equivalent to $\hat{M} = 0$ in equation (26e)),

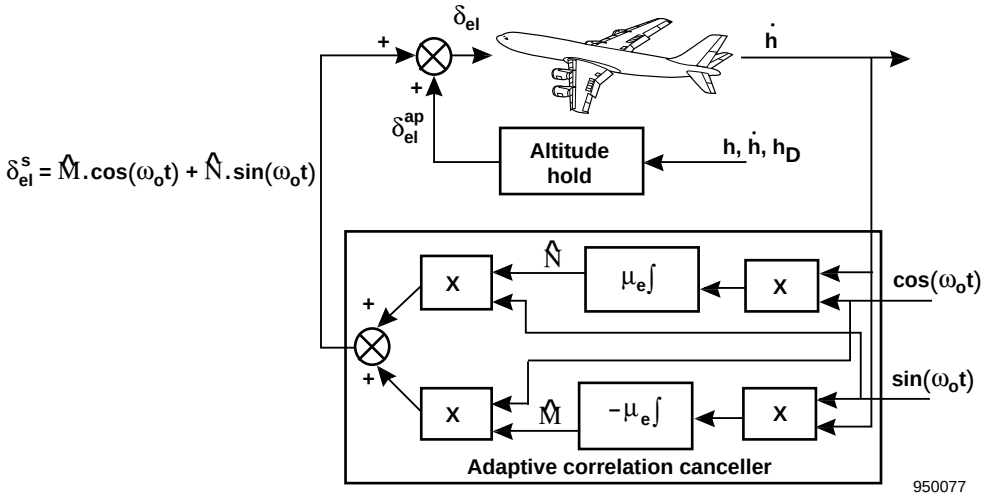

Figure 5. Adaptive constraints controller: δ_{el}^{s} signal synthesizer.

we conclude that the assumption of linearity between the effectors and h is not needed (i.e., higher harmonics do not affect the convergence process) for the optimizer combined with ACC to reach the optimum.

Consequently, the algorithm (26) is expected to work well with actuators involving such nonlinear elements as position or rate saturations, hysteresis, dead bands, and nonlinear time delays. Equation (26f) shows that, upon convergence, $\dot{h}$ is also uncorrelated with respect to $\cos(\omega_o t)$. This is not necessary for convergence of the optimizer, but, given that δ_s and $\cos(\omega_o t)$ are orthogonal signals, this fact has as a consequence the (theoretical) annihilation of the ω_o-oscillations in $\dot{h}$.

Results of Simulated Experiment

For purposes of demonstration, the aileron deflection, δ_{ail}, is selected as the active surface. Calculated from the trim point characteristics at the nominal flight conditions, the optimal δ_{ail} deflection has an approximated value: $\delta_{ail}^{*} = 3°$. From the aerodata the average curvature, Γ_{CD} is estimated as Γ_{CD} = 7.32E – 05 [deg^{-2}], giving for the PI average curvature the value: $\Gamma_{acc} = \bar{q}\,.\Gamma_{CD}\,S/m$ = 8.0E – 03 [ft.sec^{-2}.deg^{-2}]. Following the design criterion mentioned previously, from equation (16) we have

$$K_{ail} = \frac{4\omega_o \bar{G}_c}{\sqrt{5}A^2\Gamma_{acc}} \approx \frac{32\omega_o}{A^2} \tag{27}$$

The amplitude of the excitation signal was chosen as A = 1°. Two excitation frequencies, with a ratio 1:3, were selected to investigate the effects of the ω_o parameter. The lower value, ω_o = 0.025, was set low enough, through a trial-and-error process using the simulation, to ensure good enough rejection, by the altitude hold, of the $\dot{h}$-oscillations. For this case, it corresponds with K_{ail} = 0.79 [sec^3/ft], and only small differences in the PI with and without ACC are expected.

Figures 6(a) to 6(h) display the results. Figure 6(a) shows the corresponding increase of the true airspeed caused by an increase of the net thrust provided by the optimizer. Figure 6(b) shows the corresponding reduction of C_D. As seen by comparing the curves with and without ACC, differences in the velocity for very low excitation frequencies are only minor. From figure 6(b), however, the average C_D is slightly smaller with ACC. For the chosen ω_o, the optimizer is expected to attain the 5-percent

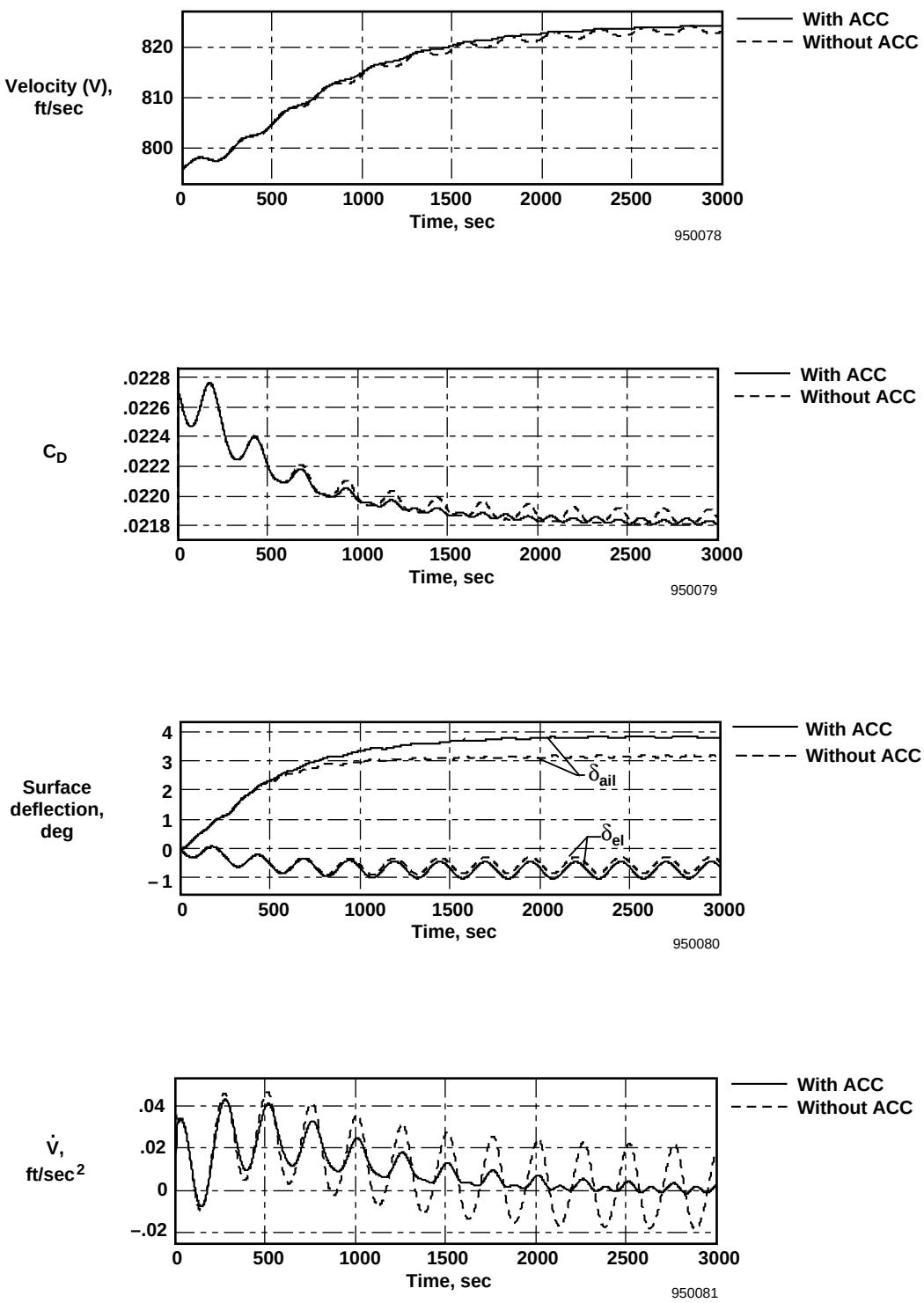

(a) through (d)

Figure 6. Velocity maximization mode; δ_{ail} is the decision variable; ω_o = 0.025.

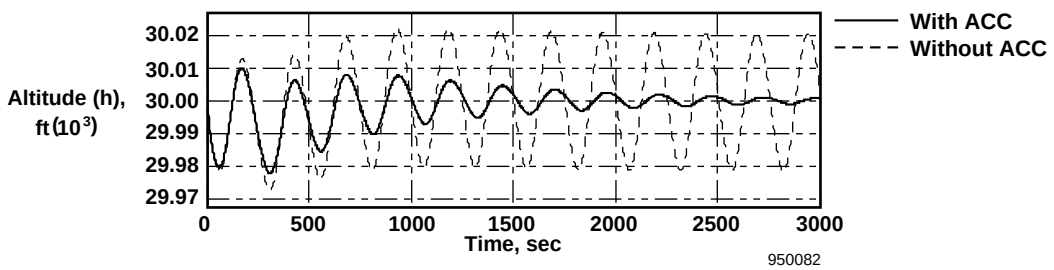

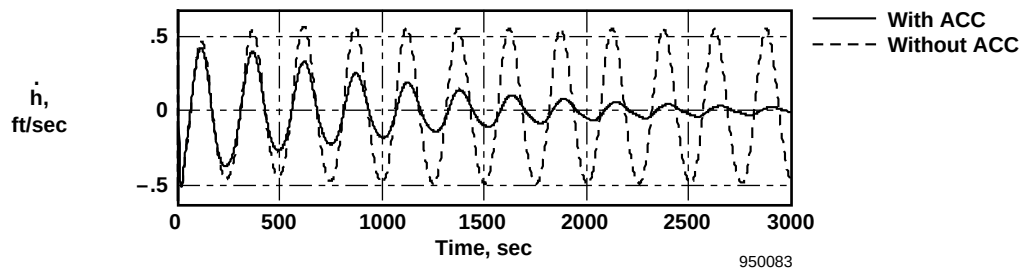

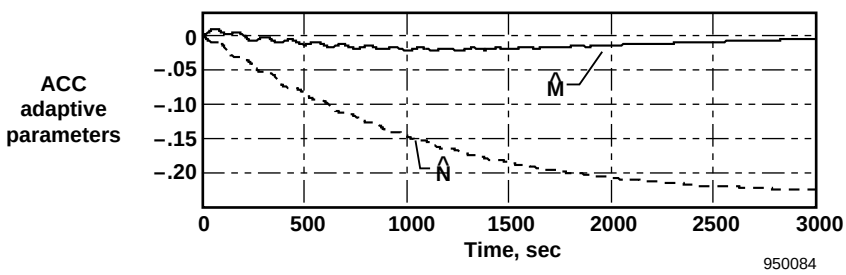

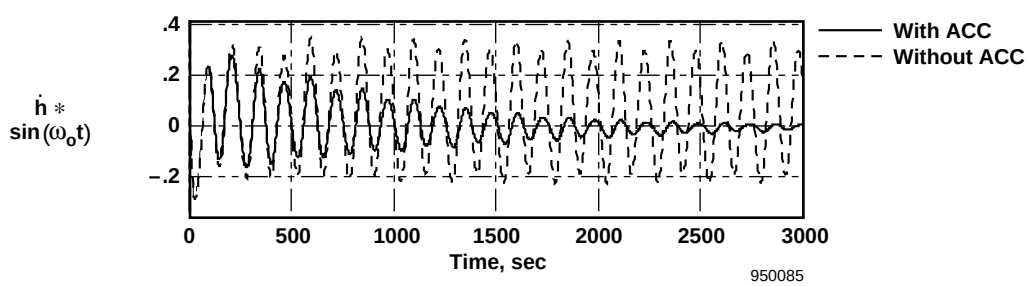

(e) through (h)

Figure (6). Concluded.

band of its final value at approximately $20/\omega_o$ = 800 sec, which is in total agreement with the plot in figure 6(c). This fact is in good agreement with the dynamic predictions provided by the analytical tools introduced previously in the Design Approach section.

The steady-state (final) aileron deflection, however, does not coincide with the optimum value determined from the characteristics (i.e., 3.8°) when ACC is not used. As shown, this lack of coincidence is the result of the constraints violations caused by the invalid assumption of an ideal autopilot (notice the ±20 ft oscillations in the altitude shown in fig. 6(e) without ACC). On the other hand, figure 6(c) shows that, with ACC, δ_{ail} converges to the optimal value: δ^*_{ail} = 3.8°. In this case, however, the dynamic cannot be predicted using the results of the Design Approach section, which do not assume the presence of ACC.

The overall dynamic now depends on the newly incorporated ACC module whose dynamic is implicitly determined by the adaptation gain, μ_e. The latter gain was chosen as μ_e = 0.001 for these experiments. Figure 6(g) displays the time history of the $\hat{M}$ and $\hat{N}$ parameters. Figure 6(f) illustrates the real effect introduced by ACC; namely, a dramatic reduction in the oscillations of $\dot{h}$ after the adaptation period. While this adaptation is performed, notice how the surface deflections with ACC depart from those without ACC (fig. 6(c) also displays the corresponding δ_{el} deflections for both with and without ACC cases).

Notice, comparing figures 6(c), 6(f), and 6(g), how the correction towards the final (optimal) value δ^*_{ail} parallels the convergence of ACC and corresponding asymptotic elimination of the oscillations in $\dot{h}$. The effects on $\dot{V}$ shown in figure 6(d) are also of interest. The algorithm with ACC reduces the oscillations on $\dot{V}$ mostly eliminating the first harmonic. The fact that only the second harmonic subsists in $\dot{V}$ and C_D (fig. 6(b)) is a direct result of attaining an extremum for the acceleration coincident with drag minimization. From the plots shown in figures 6(h), the product, $\dot{h}\sin(\omega_o t)$ has a nonzero average without ACC, indicating correlation between both signals. This correlation, as predicted, is responsible for the optimization offset. The curves with ACC demonstrate, on the other hand, how ACC asymptotically eliminates this correlation. Figure 6(e) shows the effects of ACC on the altitude oscillations.

The effects of a lack of an appropriate constraint control are accentuated when higher excitation frequencies are used. Figures 7(a) through 7(h) show simulated results for ω_o = 0.075 and corresponding gain K_{ail} = 2.4[sec^3/ft]. In particular, figures 7(a) and 7(b) show that, without ACC, performance may even be degraded (decrease in V, net increase in C_D) with respect to the nonoptimized case. This degradation results from a large offset between the optimum and the actual convergence value of the optimizer, as figure 7(c) shows. Notice, nevertheless, in figure 7(c) that, without ACC, the 5-percent convergence time is approximately equal to 20/0.075 = 266 sec, showing that the dynamic behavior is still, as theoretically predicted, three times faster than with ω_o = 0.025.

As stated before, the increase in convergence speed is not apparent when the ACC is adapted simultaneously with the optimization. By starting the ACC with pretuned parameters, the effects of ACC dynamics on the optimization are sensibly reduced. Under these conditions, the predicted dynamic (from the Design Analysis section) comes closer to the actual results (the bold lines in figs. 7(a) to (c)), featuring three times faster responses of the surface deflections (compare fig. 7(c) with 6(c)). For this experiment, however, in comparing the optimizer that has pretuned ACC with that with zero ACC initial parameters, we notice that the airspeed improves only slightly within the time horizon shown.

We now make an important distinction between attaining the optimal surface configuration and attaining the maximum speed. In fact, even after the configuration has been optimized, the newly

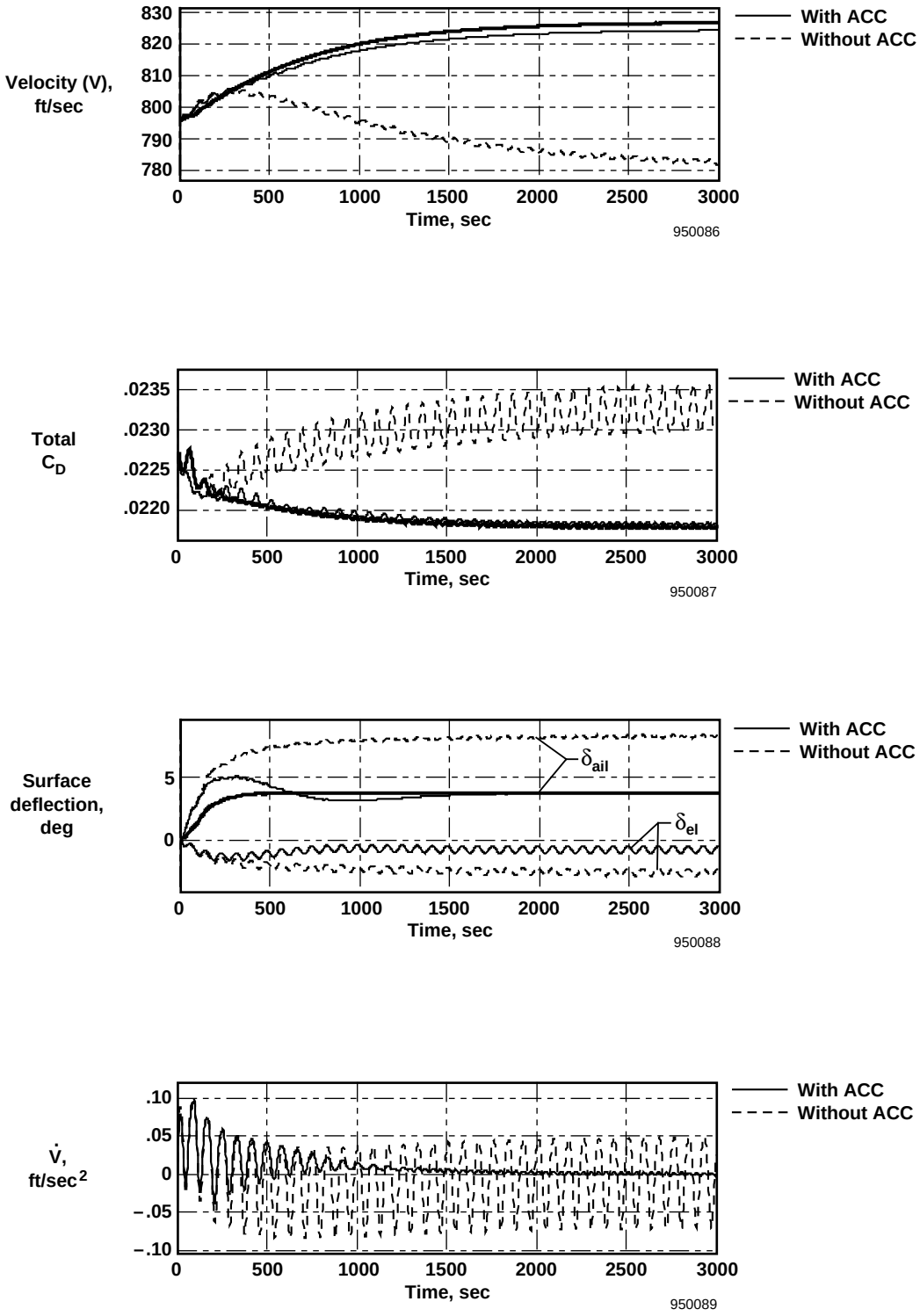

(a) through (d)

Figure 7. Velocity maximization mode; δ_{ail} is the decision variable; ω_o = 0.075.

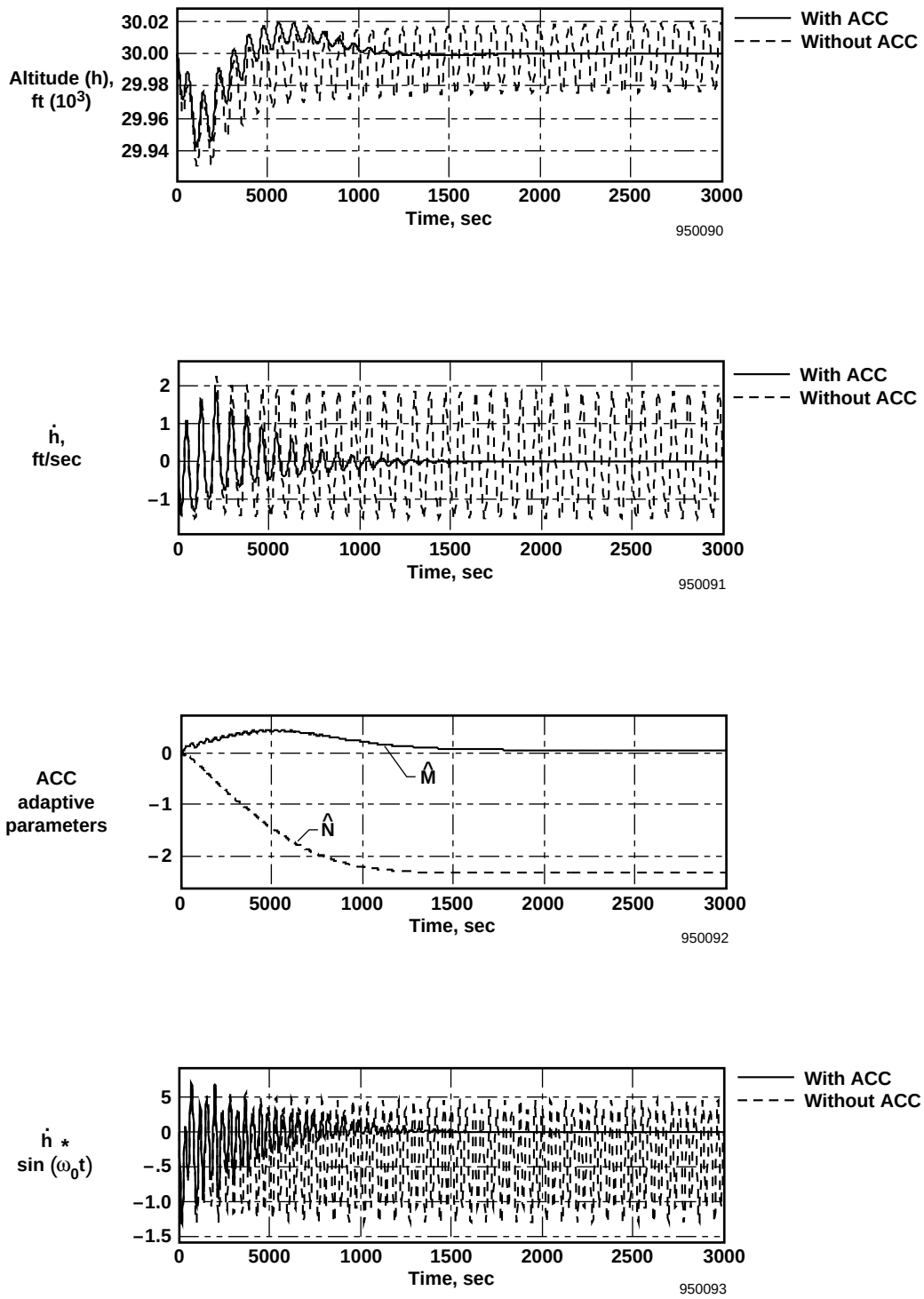

(e) through (h)

Figure 7. Concluded.

available excess thrust causes the aircraft to continue to accelerate. Dynamic pressure and Mach number effects later stop the speed increase. The slow diminution in C_D, seen after the optimization, parallels a slow average diminution in the angle-of-attack speed increase (more speed, more lift, and thus less α and C_D) not shown in the figures.

The rest of the plots in figures 7(a) through 7(h) are similar to those in figures 6(a) through 6(h). Comparing both sets of figures, we see that the increase in ω_o produced larger $\dot{h}$ oscillations (fig. 7(e)) and a stronger correlation between $\dot{h}$ and δ_{ail} (fig. 7(h)); both effects are responsible for the larger deflection offset when ACC is not used.

This simulated experiment shows that the proposed approach may improve the optimization convergence speed (through a faster excitation) without degrading the accuracy. Similar significant improvements were obtained with experiments involving symmetric flaps as the decision variable or the combination stabilator–elevator as the pitch-compensating actuator. In the latter case, the stabilator was driven by a constant-speed motor with a dead band in its control loop. In spite of these nonlinearities, the algorithm featured a perfect convergence to the optimal stabilator/aileron configuration.

Single-Surface Fuel-Flow Minimization Mode

In the fuel-flow minimization mode, the constraints are the engaged altitude and speed. Excess thrust is kept constant (at zero) while reducing simultaneously the aerodynamic drag and engine thrust. Similar to that for the velocity maximization mode, the optimal surface configuration is such that small changes around it keep the excess thrust almost unchanged (excess-thrust extremum). Because the thrust T is affected by both PLA and the surface configuration, we assume, for small configuration changes, that it may be decomposed as $T = T_p(\mathrm{PLA}) + T_\delta(\delta_{surf})$. For the velocity optimization mode, this distinction was not needed because PLA was unchanged.

Using a correlation interpretation, a necessary condition for the optimum is that corr $\{T_\delta - D, \delta_s\} = 0$ (as before, δ_s is the small sinusoidal perturbation applied to the actuator chosen as decision variable). This condition is also sufficient for the unimodal case, which is the typical case in practice for the problem at hand. Using the fact that $T_p(\mathrm{PLA})$ is a monotone function of PLA, from the velocity equation of the longitudinal flight motion, equation (11), the optimality condition, is satisfied if simultaneously

$$\mathrm{corr}\{\dot{V}, \delta_s\} = 0 \tag{28a}$$

$$\mathrm{corr}\{\dot{h}, \delta_s\} = 0 \tag{28b}$$

$$\mathrm{corr}\{\mathrm{PLA}, \delta_s\} = 0 \tag{28c}$$

For ideal altitude and velocity holds ($\dot{h} = \dot{V} = 0$), the first two conditions (28) are automatically satisfied. As was already discussed, however, an actual practical autopilot implementation may not totally cancel the oscillations in $\dot{h}$ and $\dot{V}$. Similarly, as with the velocity optimization case, those conditions are achieved by superimposing a set of (adaptively synthesized) signals on the commands generated by the autopilot. The resulting PLA and δ_{el} commands are thus

$$\mathrm{PLA} = \mathrm{PLA}^{ap} + \mathrm{PLA}^{s} \tag{29a}$$

$$\delta_{el} = \delta_{el}^{ap} + \delta_{el}^{s} \tag{29b}$$

As before, the superscripted '*s*' indicates the synthetic signals. The superscripted '*ap*' identifies the magnitudes generated by the autopilot. The degrees-of-freedom for the constrained optimization are

δ_{surf}, PLA^s, and $\tilde{\delta}_{el}$. The magnitude $\tilde{\delta}_{el}$ is used to impose condition (28b), as in the velocity optimization case, by means of the algorithm depicted in figure 5. Two alternatives are left for δ_{surf} and PLA^s:

(1) PLA^s is used to ensure that corr $\{\dot{V}, \delta_s\} = 0$ while the optimizer searches for the surface (δ_{surf}) such that corr $\{\text{PLA}, \delta_s\} = 0$. This alternative is equivalent to choosing PLA as the measured PI.

(2) PLA^s is used to impose corr $\{\text{PLA}, \delta_s\} = 0$, while the optimizer searches for the surface configuration such that corr $\{\dot{V}, \delta_s\} = 0$. In this case, $\dot{V}$ plays the role of the PI.

The second alternative uses the same PI ($\dot{V}$) as the velocity optimization mode uses, and thus, both modes share the same optimizer. This alternative allows us to design and tune the optimizer for only one mode, preferably for the simplest one (i.e., the velocity maximization mode), and use the same design for both modes. Given this attractive characteristic, the second alternative was retained.

The adaptive constraints controller, which is used to ensure the condition corr $\{\text{PLA}, \delta_s\} = 0$, is easily obtained from the diagram of figure C–2 of appendix C by identifying PLA with y_m, u with PLA^s and letting the transfer function of channel C equal 1. The resulting structure corresponds to the original adaptive noise canceller proposed by Widrow et al. (ref. 12).

Summarizing, the adaptive fuel-flow minimization algorithm with adaptive constraints controller is given by the set of equations (26a) to (26g) combined with the following:

$$\text{PLA} = \text{PLA}^{ap} + \text{PLA}^s \tag{26h}$$

$$PLA^s = \hat{P}\cos(\omega_o t) + \hat{Q}\sin(\omega_o t) \tag{26i}$$

$$\dot{\hat{P}} = \mu_p \text{PLA}\cos(\omega_o t) \tag{26j}$$

$$\dot{\hat{Q}} = \mu_p \text{PLA}\sin(\omega_o t) \tag{26k}$$

where $\mu_p : 0 < \mu_p << 1$. Figure 8 depicts the diagram corresponding to equations (26).

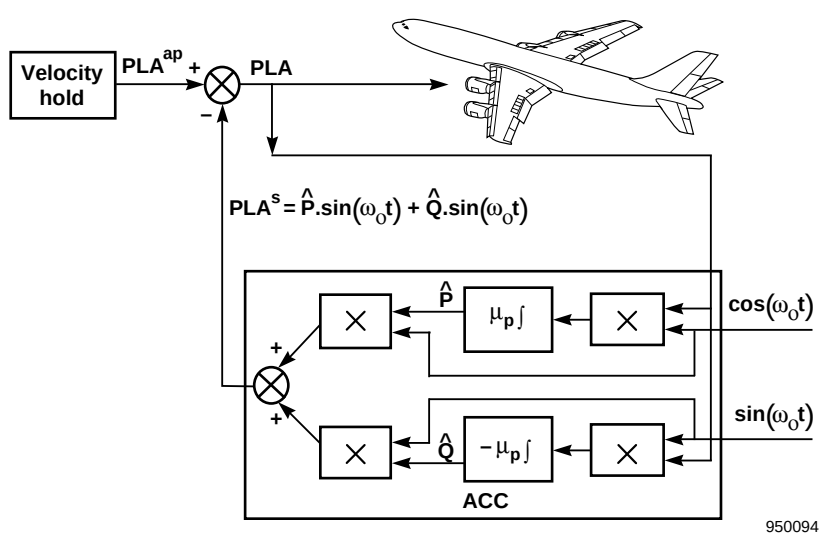

Figure: 8. Adaptive constraints controller: PLA^s signal synthesizer.

Results of Simulated Experiment

We now consider the results of the simulation tests performed for the fuel-flow minimization mode, this time using symmetric flaps deflection (instead of ailerons) as the decision variable. The nominal trim point characteristics at the given flight condition indicate that the optimal symmetric flap deflection is $\delta^*_{fl} \approx 3°$. From the aero data, Γ_{CD} was estimated as $\Gamma_{CD} = 1.4E - 05[\text{deg}^{-2}]$, and the corresponding Γ_{acc} as $\Gamma_{acc} = 15.3E - 03[\text{ft.sec}^{-2}.\text{deg}^{-2}]$. In this experiment, ω_o was chosen to equal 0.0975 rad/sec. Similarly as in the aileron optimization case, the excitation amplitude was taken as A = 1°.

Choosing the same algorithm design as for the velocity maximization mode, i.e., $\overline{G}_c = 0.1408$, we calculate $K_{fl} = 1.62[\text{sec}^3/\text{ft}]$. The expected convergence speed of the algorithm is characterized by the estimated rise-time to the 5-percent band: 20/0.0975 = 205 sec. As with the velocity maximization mode, the elevator is used to compensate for pitch moment changes. The altitude and the velocity holds were both activated. The signals synthesized by the ACC were added to those generated by the autopilot.

As discussed before, ACC for the fuel-flow minimization has two parts. The part common to the velocity maximization mode, represented in figure 5, is called here ACC1. The other part, specific for the fuel-flow minimization mode, is called ACC2 and is described by equations (26h) to (26k). Figure 9(a) shows a significant difference in the averages of the PLA (only deviations with respect to the trim value of PLA are indicated in the figure) between the cases with and without ACC.

The difference in the average is also noticeable between the cases ACC1 alone and ACC1+ACC2. Note, particularly, for the ACC1 + ACC2 case, how the first harmonics in PLA and C_D (fig. 9(b)) are totally eliminated. This fact, together with the visible presence of the second harmonics, signals the convergence of the average flap deflection to the optimum value. This result is corroborated by figure 9(c), which shows that only the ACC1 + ACC2 option tends to the *a priori* estimated optimum ($\delta^*_{fl} = 3°$), although with ACC1 only, the convergence error is still considerably smaller than without ACC. As expected, the ACC1 eliminates the oscillations in $\dot{h}$ (fig. 9(d)). This result is in agreement with those obtained for the velocity maximization mode. No further improvement is obtained in this sense with ACC2.

Figures 9(e) and 9(f) show the positive effects of ACC on the regulation of, respectively, velocity and altitude. Figures 9(d) and 9(h) demonstrate the clear-cut effect of ACC in compensating for the remnant oscillations in potential and kinetic energies. Finally, figure 9(g) shows the time evolution for the adaptive parameters, for ACC1 and ACC2. The adaptation gains for algorithms ACC1 and ACC2 were arbitrarily made 10 times higher than the one chosen for velocity maximization, i.e., $\mu_e = \mu_p = 0.01$. The intention was to show, on one hand, what effects these gains have on the adaptation speed (notice the time-scale change between figs. 9 and 6 through 7) and, on the other hand, that the choice of their value is not critical for design purposes.

Multisurface Optimization

In this section, we use the algorithm developed in previous sections to optimize, simultaneously, more than one decision variable. The decision variables considered are symmetric ailerons δ_{ail} and symmetric flaps δ_{fl}. As before, the elevator deflection and the PLA are dependent variables used to ensure the optimization constraints. Figure 10 shows the general structure of the multidecision variable optimization.

Two frequencies, $\omega_{ail} = 0.075$ and $\omega_{fl} = 0.0975$, are used for the independent excitation signals δ_{s1} and δ_{s2}, respectively, added to the command signals δ_{ail} and δ_{fl}. The ratio $\omega_{fl}/\omega_{ail} = 1.3$ is chosen to avoid possible low harmonic resonances. Each optimizer loop has its corresponding set of ACC1 and ACC2

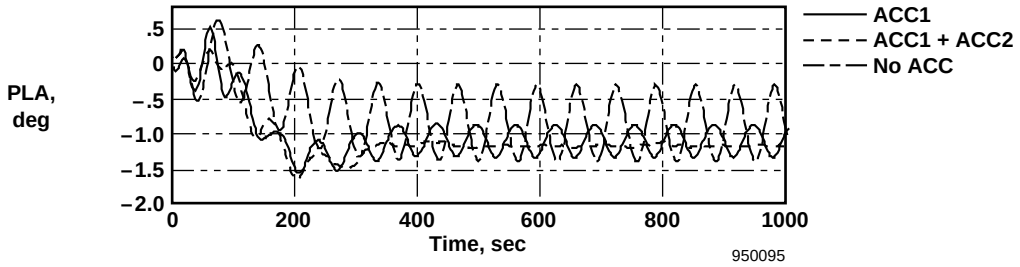

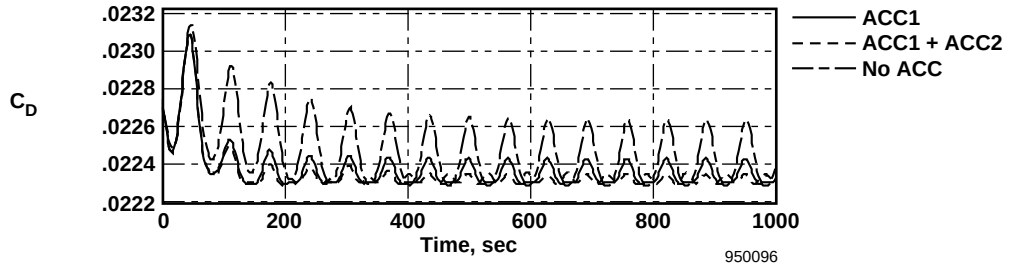

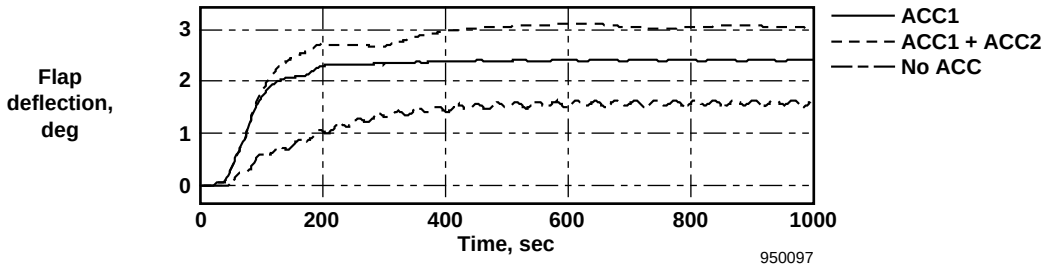

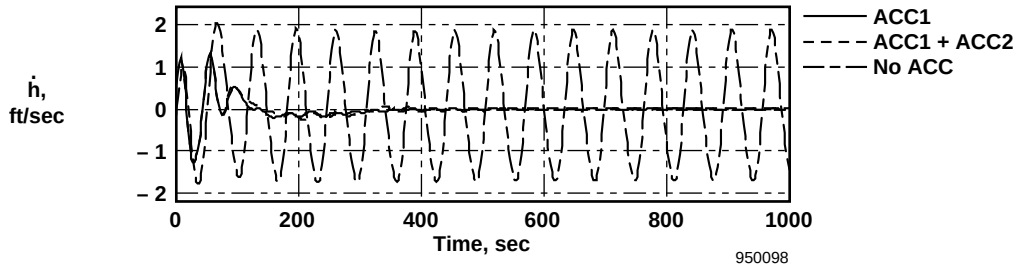

(a) through (d)

Figure 9. Fuel-flow minimization mode; δ_{fl} is the decision variable; ω_o = 0.0975.

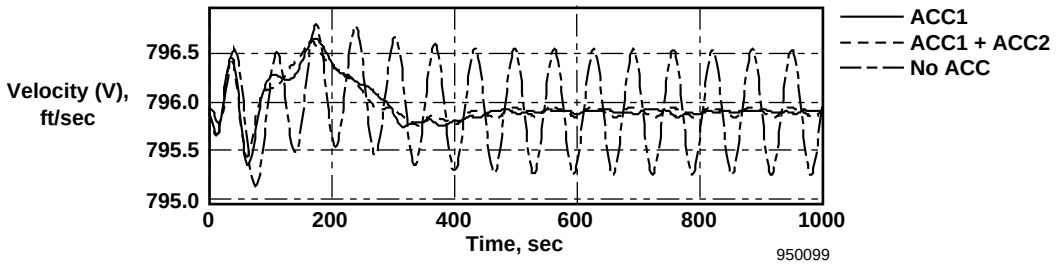

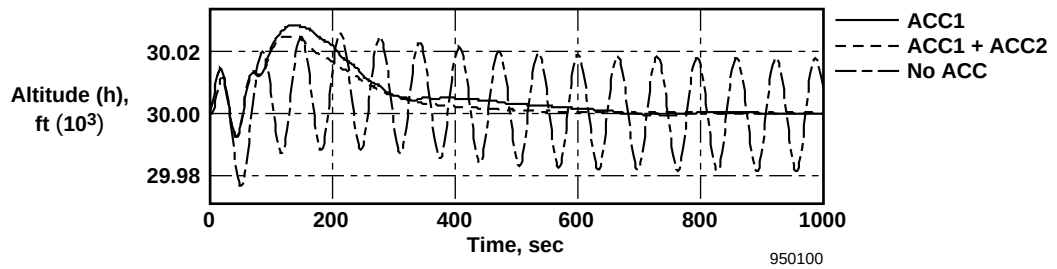

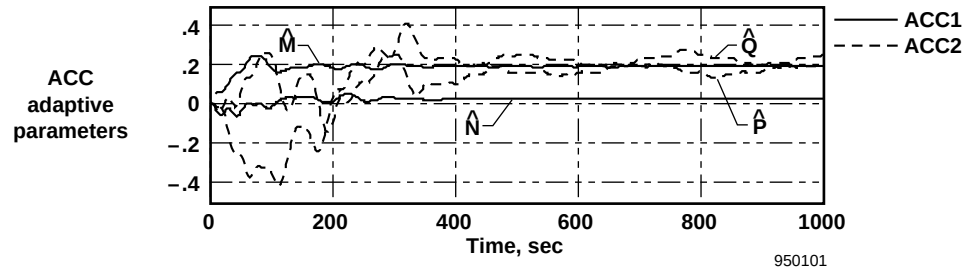

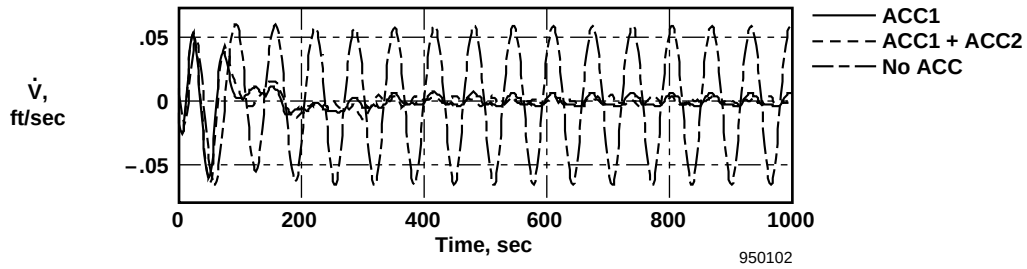

(e) through (h)

Figure 9. Concluded.

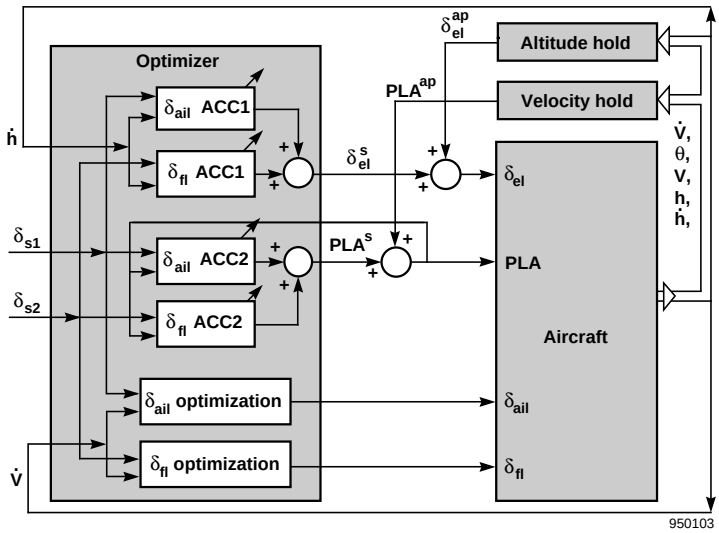

Figure 10. Multivariable optimizer.

modules. Each loop is designed independently, following the guidelines presented in the previous sections. The corresponding adaptation gains are K_{ail} = 2.4[sec^3/ft] and K_{fl} = 1.62[sec^3/ft]. The gains for ACCs in both loops are selected as $\mu_e = \mu_p = 0.005$.

Velocity Optimization Mode: Results of Simulation Experiment

Figure 11 shows the results for the multisurface velocity optimization mode. Two cases are considered: (1) with pretuning of ACC parameters (i.e., the initial condition of adaptive ACC parameters set equal to the final values of a previous optimization), $\hat{M}_{ail}$ and $\hat{N}_{ail}$ for the aileron loop and $\hat{M}_{fl}$, and $\hat{N}_{fl}$ for the flap loop; (2) without pretuning of the ACC parameters, (i.e., all initial conditions are set equal to zero and the ACC parameters are adapted simultaneously with the optimization).

As can be seen from figures 11(a) and 11(b), the difference between both cases in the airspeed and total C_D coefficient is almost unnoticeable. Compared with the single-surface optimization cases, a higher final speed and lower C_D coefficients are attained in the multivariable case. Figures 11(c) and 11(d) show the time history of the surface deflections. The deflections appear to converge to approximately the same values as those in the single-surface optimization case, suggesting only a light coupling among the optimization variables. With pretuned ACC parameters, the surface deflections show better transient behavior. Thus, a smoother transient on the magnitudes is depicted in figures 11(e) to 11(g). The same figures show, consistent with the algorithm's expected asymptotic behavior, that, independently of the initial condition, the time history of both cases tends to converge toward each other. Finally, figures 11(h), and 11(i) show the time history of the ACC parameters with and without pretuning.

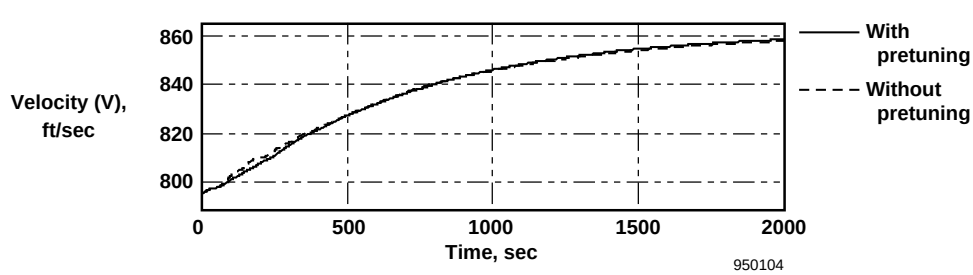

(a)

Figure 11. Multisurface velocity optimization mode with and without pretuning of the ACC parameters.

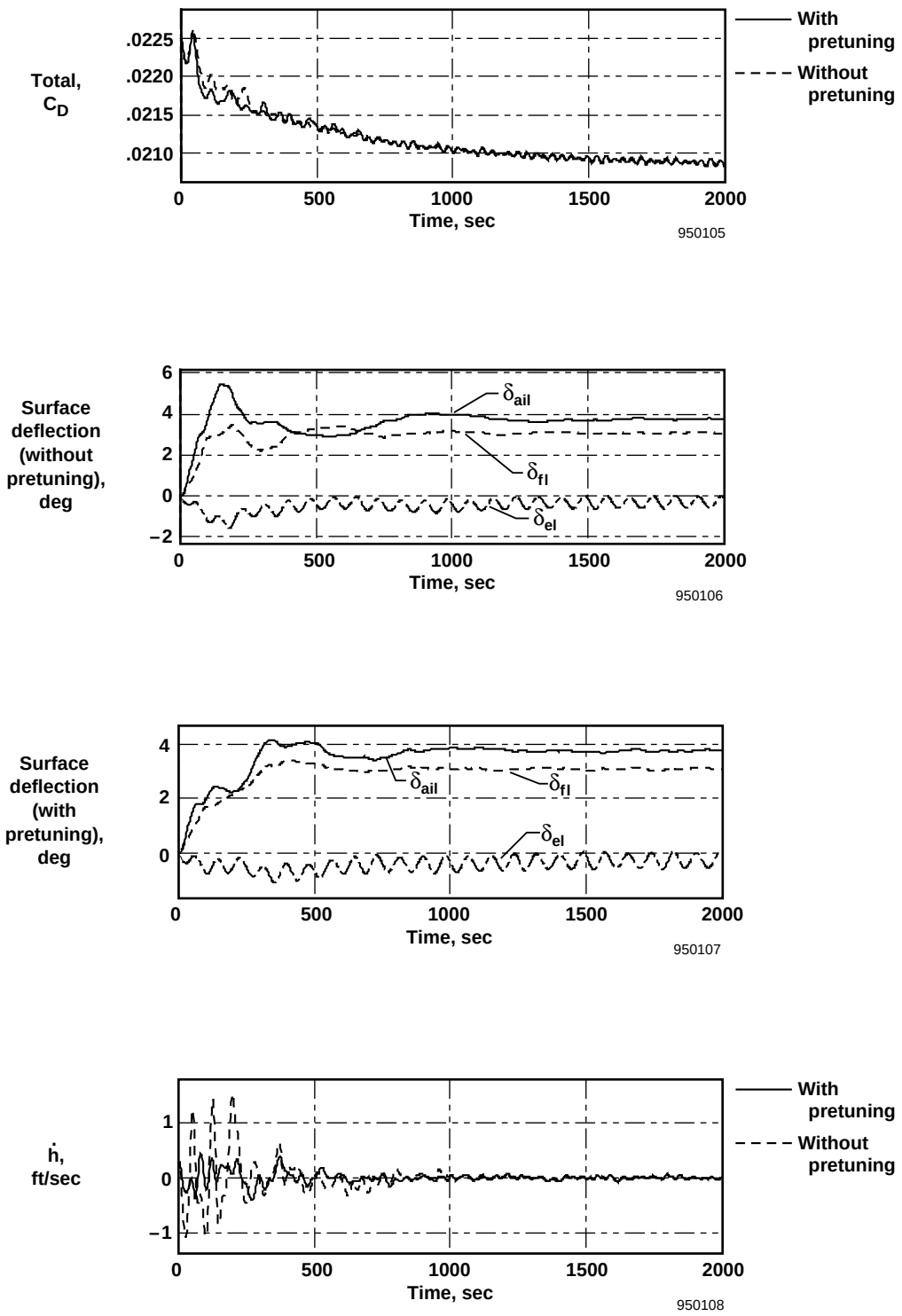

(b) through (e)

Figure 11. Continued

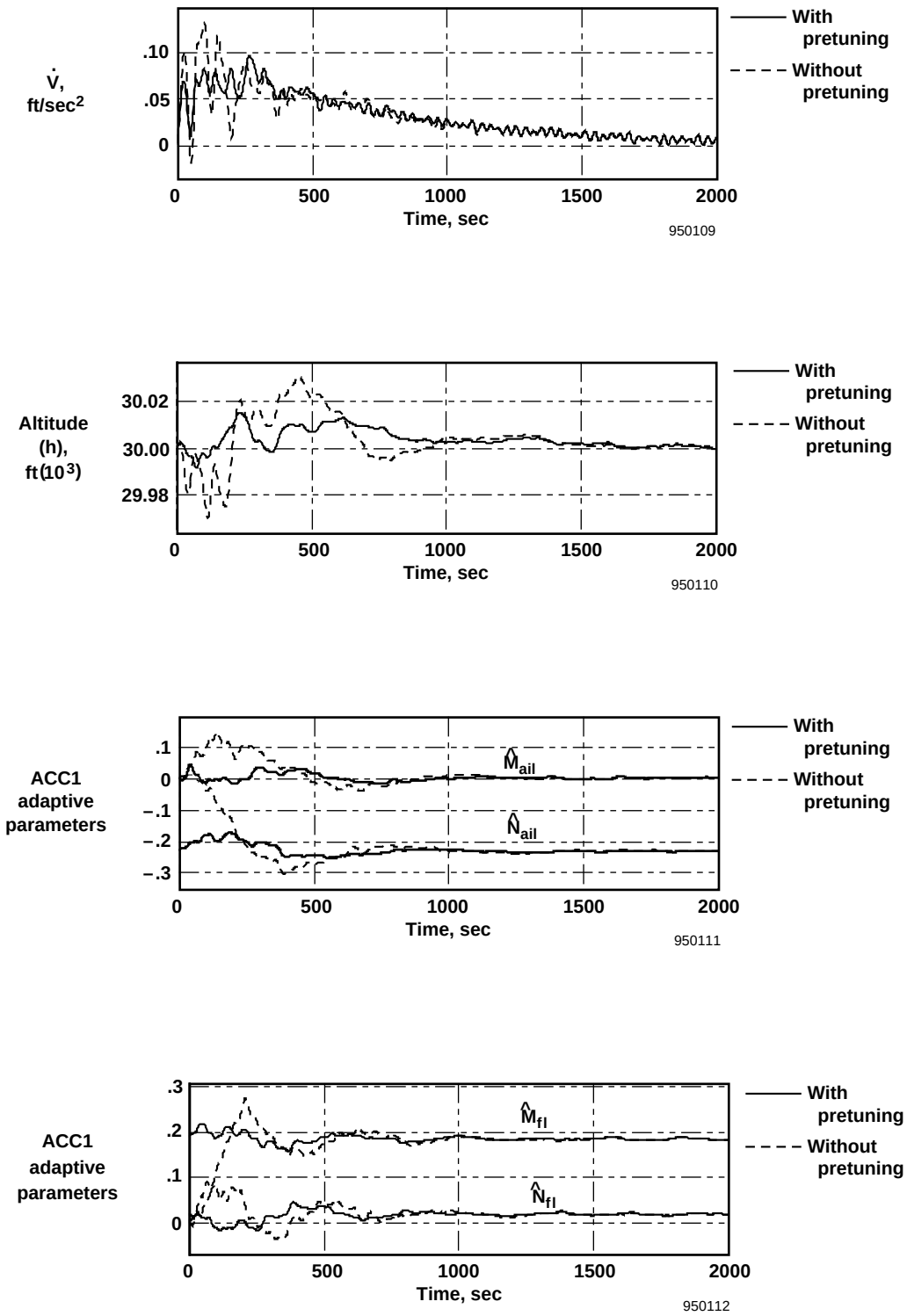

(f) through (i)

Figure 11. Concluded.

Fuel-Flow Optimization Mode: Results of Simulation Experiment

Figure 12 shows the corresponding results for this mode. Figures 12(a) and 12(b) show a PLA reduction along with a reduction in the total C_D coefficient. As expected, the transient behavior is improved when the ACC parameters are pretuned. This improvement is also reflected in a sensible reduction of the excursions in the decision variables δ_{ail}, and δ_{fl} (figs. 12(c) and 12(d)) and an improved transient behavior for the variables shown in figures 12(e) through 12(h). Again, only the transient behavior is affected with pretuning, while, asymptotically, the pretuned and nonpretuned cases are indistinguishable.

Figures 12(i) to 12(l) show the adaptive parameters $\hat{M}$, $\hat{N}$, $\hat{P}$, and $\hat{Q}$. Notice how the learning period of these constants approximately coincides with the bad transient period in figures 12(e) through (h). This fact justifies the use of prelearned values of the $\hat{M}$, $\hat{N}$, $\hat{P}$, and $\hat{Q}$ stored in memory as future initial conditions for the optimization algorithm. Those values, taken from a previous optimization (or resulting from a purely in-flight identification trial without optimization) at the given flight condition, are considered the best available characterizing the actual aircraft and flight condition.

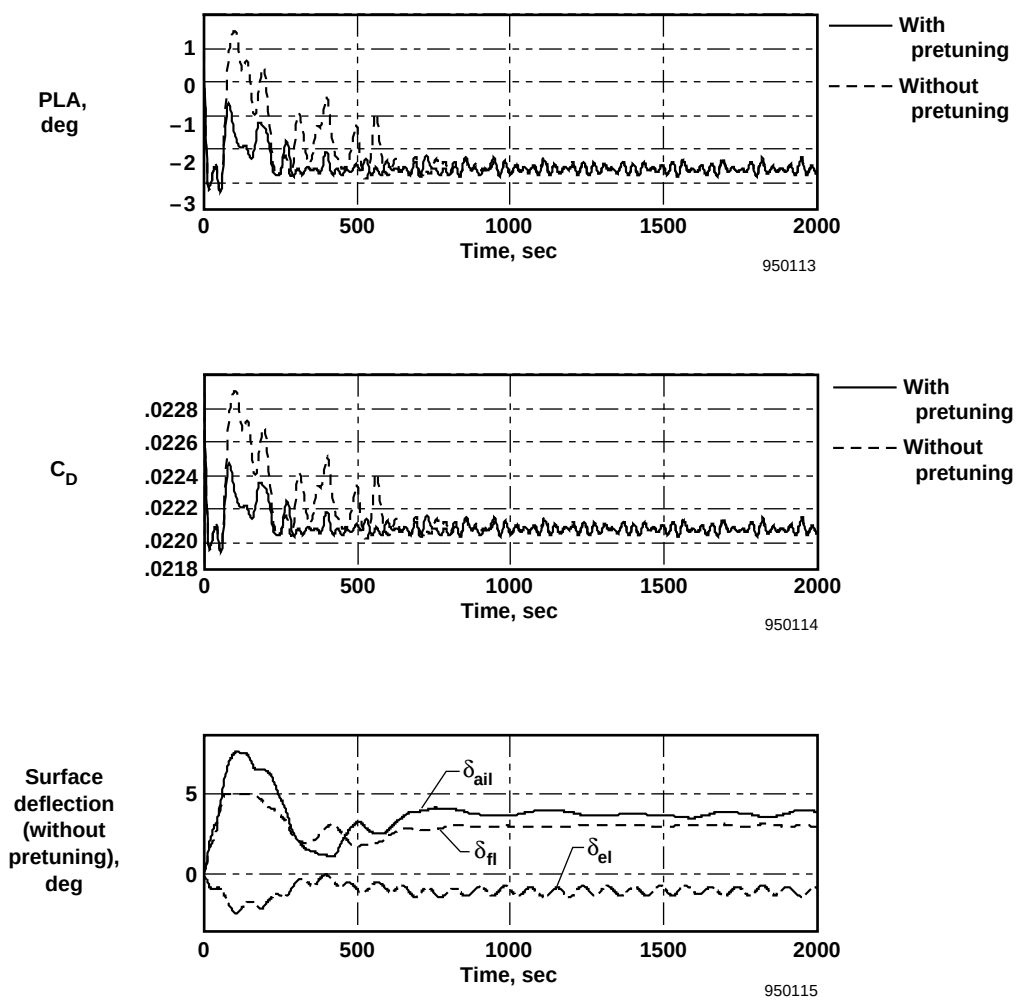

(a) through (c)

Figure 12. Multisurface fuel-flow optimization mode with and without pretuning of the ACC parameters.

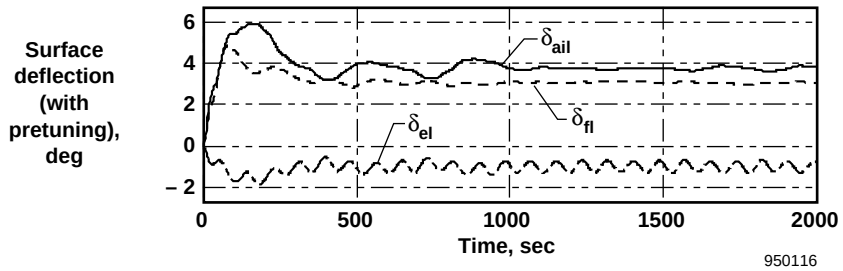

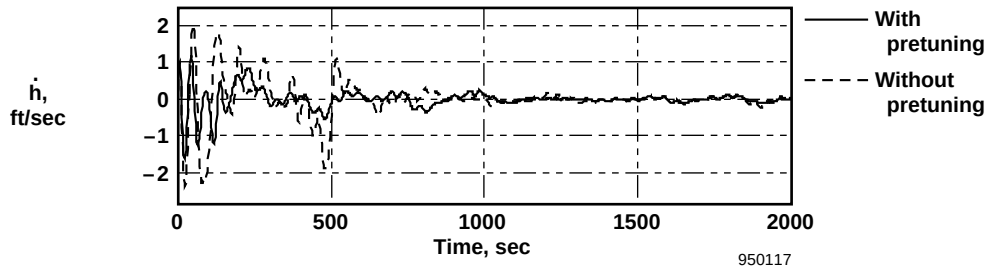

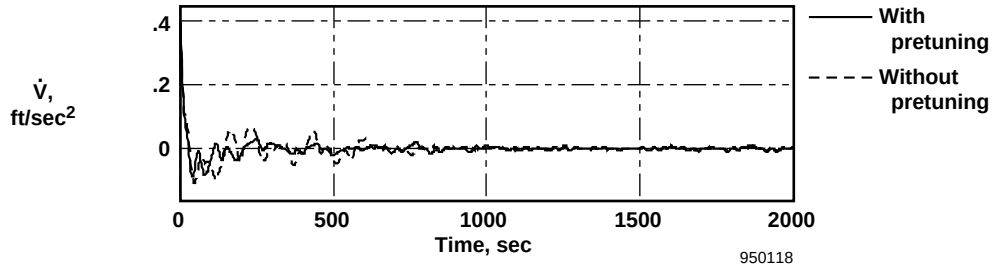

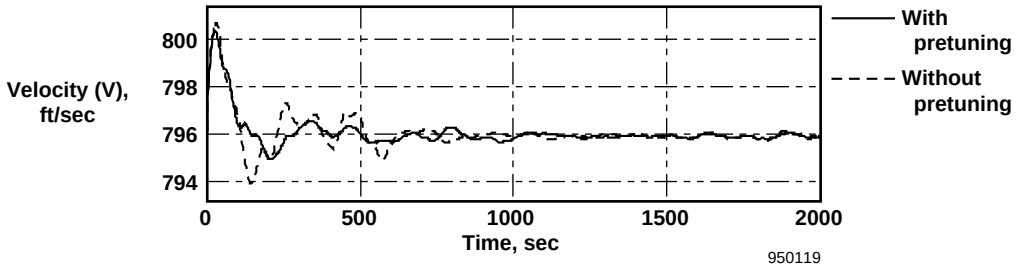

(d) through (g)

Figure 12. Continued

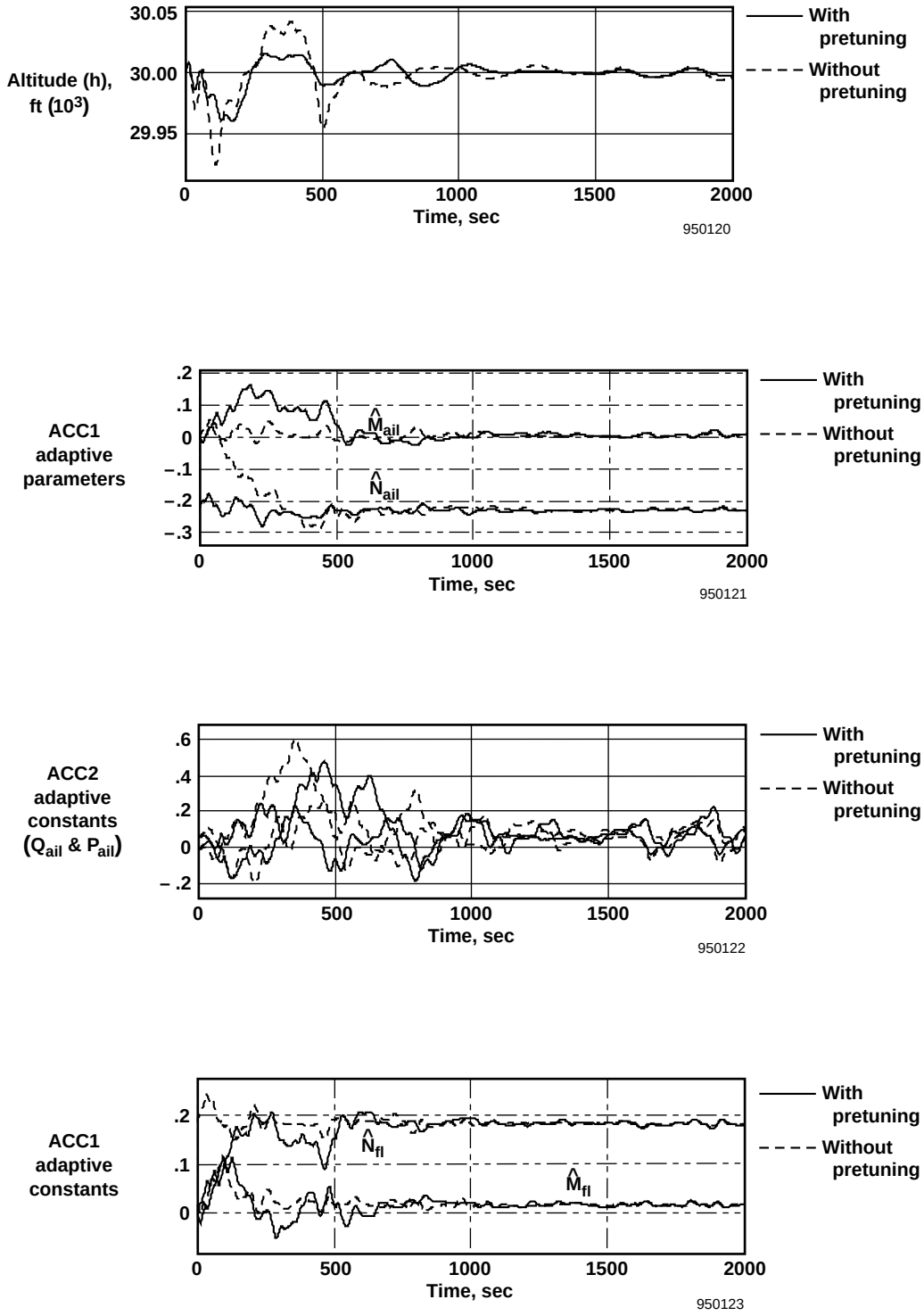

(h) through (k)

Figure 12. Continued

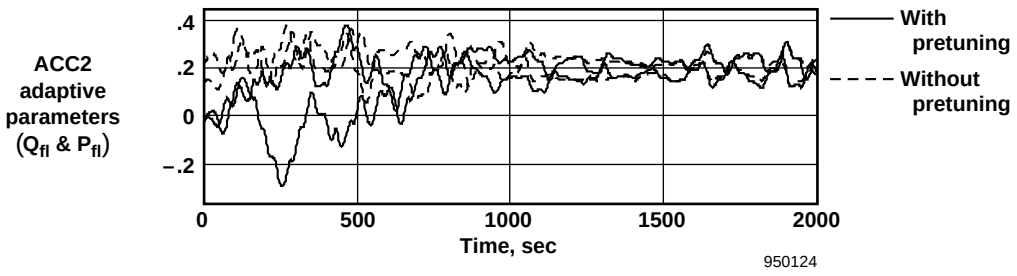

(l)

Figure 12. Concluded.

Concluding Remarks

An adaptive perturbational technique for in-flight performance optimization of a transport aircraft is proposed and demonstrated for a simulated B-720 aircraft. The technique is simple and easy to design and implement in an onboard computer. When applied to the combined system autopilot–aircraft as an external loop, the technique requires no *a priori* knowledge of the autopilot design. The aircraft may be optimized at its actual flight condition, characterized by altitude, speed, weight, center-of-gravity position, actual engine characteristics, and aircraft age.

The algorithm is robust with respect to any *a priori* information used for its design as well as changing flight conditions. Noise, external disturbances (such as those coming from changing atmospheric conditions), and measurement biases are naturally rejected by the algorithm whose working principle is based on online cross-correlation measurements between decision variables and a performance index.

The same index (i.e., the horizontal acceleration) is used for the speed-maximization mode and for fuel-flow minimization mode; this is because both modes are particular cases of an excess-thrust maximization problem. Both modes share a major part of the algorithm. Moreover, the speed-maximization mode algorithm is a submodule of the fuel-flow minimization mode. This fact adds modularity and alternative ways to check the same algorithm.

The effects of the probing disturbances on the optimization constraints are compensated with an adaptive feed-forward loop called an adaptive constraints controller (ACC). The ACC allows for a faster optimization than was possible previously by using the autopilot as the only constraint controller device. More importantly, it prevents offsets with respect to the optimal decision variables. With the ACC complementing the autopilot’s constraints-control capabilities, the optimizer takes full advantage of the autopilot’s action, but without requiring any information on the autopilot design.

A straightforward extension of the single-variable design was used for multivariable optimization. The multisurface optimization problem that was simulated seems to be somewhat decoupled. This fact favors the convergence and dynamic properties of the steepest-descent type of algorithm used. Were the problem at hand more coupled, an upgrade of the present version to a second-order one, such as a quasi-Newton method, would help the convergence speed in the multivariable optimization case. More research is necessary to ascertain whether this path is necessary, for instance, in an integrated airframe propulsion optimization context. The good results obtained so far for the multivariable case encourage a pursuit of that avenue with the proposed algorithm.

The theory developed is sound, and the resulting algorithm exhibits good dynamic and convergence properties. Moreover, the simulation results show the algorithm's potential for handling complex multivariable performance optimization problems. The algorithm is a suitable candidate for in-flight integrated airframe–engine optimization. However, to apply the proposed approach requires a determination of small sensitivity levels under realistic cruise flight conditions of transport aircraft. The continued development of this technology requires algorithm evaluation in a high-fidelity simulation (similar to those used for FAA-certified pilot training), followed by a flight test program validation of the technology. A successful flight demonstration of the technology is required before potential users and beneficiaries will commit resources to implement the technology in new aircraft designs or retrofit programs.

References

1. "Aeronautical Technologies for the Twenty-First Century," Committee on Aeronautical Technologies, Aeronautics and Space Engineering Board, National Research Council, National Academic Press, Washington, DC, 1992.

2. Phillips, P. W. and S. B. Smith, "AFTI/F-111 Mission Adaptive Wings (MAW) Automatic Flight Control System Modes Lift And Drag Characteristics," AFFTC-TR-89-03, May 1989.

3. Renken, J., "Mission-Adaptive Wing Camber Control Systems For Transport Aircraft," AIAA-85-5006, 1985.

4. "New Large Aircraft." *Flight International*, November 24–30,1993, pp. 34–36.

5. Gilyard G. and M. España. *On the use of Controls for Subsonic Transport Performance Improvement: Overview and Future Directions*, NASA TM-4605, August 1994.

6. Eveleigh, V. W., *Adaptive Control and Optimization Techniques*, McGraw-Hill Book Co., New York, 1967.

7. Draper, C. S. and Y. T. Li, *"Principles of Optimalizing Control Systems:* An Application to the Internal Combustion Engine,*"* Research report, Aeronautical Engineering Department, Massachusetts Institute of Technology, September 1951.

8. Gilyard, G. B. and J. S. Orme, *Performance Seeking Control: Program Overview and Future Directions*, NASA TM-4531, August 1993.

9. España, M. D. and G. B. Gilyard, *On the Estimation Algorithm Used in Adaptive Performance Optimization of Turbofan Engines*, NASA TM-4551, December 1993.

10. España, M. D., "Sensor Biases Effect on the Estimation Algorithm for Performance-Seeking Controllers," *AIAA. Propulsion and Power*, vol. 10, no. 4, July/August 1994, pp. 527–532.

11. Stevens, B. L. and F. L. Lewis, *Aircraft Control and Simulation*, John Wiley & Sons, Inc., New York, 1992.

12. Widrow, B. J., J. R. Glover, Jr., J. M. McCool, J. Kaunitz, C. S. Williams, R. H. Hearn, J. R. Zeidler, E. Dong, Jr., and R. C. Goodlin, "*Adaptive Noise Canceling: Principles and Applications," Proc. IEEE*, vol. 63, no. 12, December 1975, pp. 1692–1716.

13. Goodwin C. G. and K. S. Sin, "*Adaptive Filtering Prediction and Control,"* Prentice-Hall, Inc., Englewood Cliffs, New Jersey, 1984.

14. España, M. and G. Gilyard, "Adaptive Wing Camber Optimization: a Periodic Perturbation Approach," 13th IFAC Symposium on Automatic Control in Aerospace, Palo Alto, California, September 1994.

Appendix A

Sample Calculation of an Envelope Equivalent Transfer Function

As a sample calculation of an envelope equivalent transfer function, the calculations corresponding to the first-order system are

$$G(s) = \frac{K}{s + p} \tag{A1}$$

The parameters for the envelope equivalent system are calculated as

$$\beta = \left|G(j\omega_o)\right| = \frac{K}{p(1 + \omega_o^2 / p^2)^{1/2}} \tag{A2}$$

$$\varphi(\omega) = -\text{arc tan}(\omega / p) \Rightarrow \tau = -\left.\frac{\partial\varphi(\omega)}{\partial\omega}\right|_{\omega = \omega_o} = \frac{1}{p(1 + \omega_o^2 / p^2)} \tag{A3}$$

This gives the following equivalent transfer function:

$$G_e(s) = \frac{K(1 + \omega_o^2 / p^2)^{1/2}}{s + p(1 + \omega_o^2 / p^2)} \tag{A4}$$

Appendix B

Optimization Offset Caused by Constraints Violations

To show equation (17a), we start from the equations of the longitudinal flight motion:

$$m\dot{V} = T\cos\alpha - D - mg\sin\gamma \tag{B1}$$

$$\dot{h} = V\sin\gamma \tag{B2}$$

As seen in the discussion of property P3 (eq. (7)), if δ_s is the periodic excitation signal (i.e., $\delta_s = A\sin\omega_o t$), the necessary condition for convergence of the optimizer algorithm in the velocity mode is

$$\mathrm{corr}\{\dot{V}, \delta_s\} = 0 \tag{B3}$$

When the constraint is satisfied, $\dot{h} = 0$ from (B1) we have the desired result, i.e.,

$$\mathrm{corr}\{T\cos(\alpha) - D, \delta_s\} = 0 \tag{B4}$$

However, if the constraint is not satisfied, instead of equation (B4) we have the condition

$$\begin{gathered}\mathrm{corr}\{\dot{V},\delta_s\} = 0 \Rightarrow \\ \mathrm{corr}\{T\cos(\alpha) - D,\delta_s\} = \mathrm{corr}\{mg\ \dot{h}/V,\delta_s\} = \mathrm{corr}\{\dot{E}_p/V,\ \delta_s\}\end{gathered} \tag{B5}$$

that we approximate by (see footnote on p. 6)

$$\mathrm{corr}\{D, \delta_s\} \cong -\mathrm{corr}\dot{E}_p/V, \delta_s \tag{B6}$$

On the other hand, assuming for D the expression:

$$D = D_o + \frac{\Gamma_D}{2}(\delta - \delta^*)^2 \tag{B7}$$

with $\Gamma_D := \bar{q}\, S\Gamma_{CD}$, and following a development similar to that used in the Design Analysis section to obtain equation (6), the left-hand side of (B6) turns into

$$\mathrm{corr}\{\delta_s, D\} = \frac{A^2\Gamma_D}{2}(\delta - \delta^*) \tag{B8}$$

Equations (17) are thus obtained substituting (B8) into (B6).
Now, using the approximation valid for almost leveled flight: $\sin(\gamma) \cong \gamma$, between (B2) and (B6) we have

$$\delta^\infty - \delta^* \cong -\frac{2mg}{\Gamma_D A^2}\mathrm{corr}\{\gamma, \delta_s\} \tag{B9}$$

Besides, by definition of $G_\gamma(j\omega_o)$, the ω_o-component of $\gamma(t)$ is $|G_\gamma(j\omega_o)|A\sin(\omega_o t + \varphi_\gamma(j\omega_o))$, which, correlated with $\delta_s(t) = A\sin(\omega_o t)$, gives

$$\delta^\infty - \delta^* = -\frac{2mg}{\Gamma_D}|G_\gamma(j\omega_o)|\mathrm{corr}\{\sin(\omega_o t), \sin(\omega_o t + \varphi_\gamma(j\omega_o))\} \tag{B10}$$

From (B10) follows equation (18) using a standard result of correlations between sinusoidal signals (see expression (5) in the main text).

Appendix C

Adaptive Rejection of a Sinusoidal Disturbance

The problem of a disturbance rejection from a measured physical magnitude of interest is posed as follows. In figure C–1, y is the useful signal perturbed by the disturbance d. From the available measurement y_m, it is desired to remove the effects of d and thus recover the original signal y. For this objective, an independent input u, going through the channel C, is available. C is assumed to be linear but with unknown transfer function $G(s)$. The signal d is a sinusoidal signal with known frequency ω_o but unknown phase and amplitude. It is assumed that ω_o does not lie in the spectrum of y. The objective is to design the adaptive signal synthesizer block that generates the required signal u so that $\hat{d}$ has the appropriate phase and magnitude to cancel out the effects of d on y_m. Using notation introduced in the main text we write

$$u(t) = \hat{M}\cos(\omega_o t) + \hat{N}\sin(\omega_o t) = \hat{U}^T\eta \tag{C1a}$$

$$d(t) = A\cos(\omega_o t) + B\sin(\omega_o t) := D^T\eta \tag{C1b}$$

$$\hat{d}(t) = \left|G(j\omega_o)\right|(\hat{M}\cos(\omega_o t + \psi) + \hat{N}\sin(\omega_o t + \psi)), \tag{C1c}$$

Equation (C1c) can also be written in the more compact form:

$$\hat{d}(t) = \left|G(j\omega_o)\right|\hat{U}^T R_\psi \eta(t) = \left|G(j\omega_o)\right|(R_{-\psi}\hat{U})^T\eta(t), \tag{C2}$$

where

$$R_\psi := \begin{bmatrix} \cos(\psi) & -\sin(\psi) \\ \sin(\psi) & \cos(\psi) \end{bmatrix} \tag{C3}$$

is the ψ-rotation matrix and $R_{-\psi}$ its inverse (or transpose given its orthogonality). We now define:

$$e := d + \hat{d} = (D + \left|G(j\omega_o)\right|R_{-\psi}\hat{U}(t))^T\eta(t) := \theta^T(t)\eta(t) \tag{C4}$$

$$\theta(t) := D + \left|G(j\omega_o)\right|R_{-\psi}\hat{U}(t) \tag{C5}$$

We are looking for $\hat{U}(t)$ such that $\theta(t) \to 0$ (and consequently $e(t) \to 0$). Accordingly, we first define the matrix Q and the function L as

$$L(t) = \frac{1}{2}\theta^T(t)Q\theta(t), \; Q = \frac{1}{\left|G(j\omega_o)\right|}R_\psi \tag{C6}$$

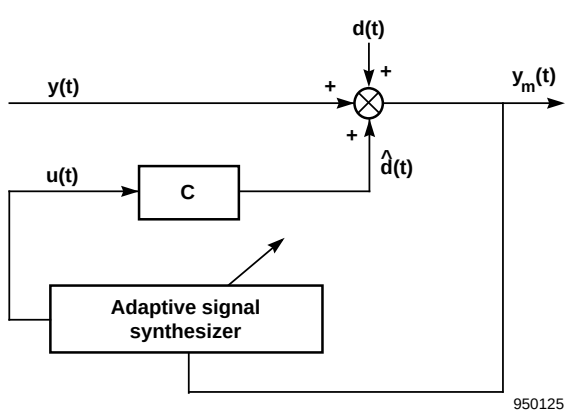

Figure C–1. Adaptive disturbance rejection scheme.

For $\left|G(j\omega_o)\right| \neq 0$, $Q > 0$, if and only if $\psi \in (-\pi/2, \pi/2)$ (rotation less that 90°) and $L(t)$ is thus a strictly positive function of time. From (C5) and (C6) we now calculate

$$\dot{L}(t) = \theta(t)^T Q \dot{\theta}(t) = \theta^T \dot{\hat{U}}(t) \tag{C7}$$

and letting

$$\dot{\hat{U}}(t) = -\mu e \eta(t) \tag{C8}$$

with μ a positive constant we have

$$\dot{L}(t) = -\mu e^2 < 0 \tag{C9}$$

Because η is, by definition, a bounded continuous function, from (C3), (C6), and (C9) we necessarily have $e \to 0$ and $\theta \to 0 \Rightarrow \hat{U}(t) \to -\left|G(j\omega_o)\right|^{-1} R_\psi D$.

For $|\psi| \approx \pi/2$, small changes in ψ may prevent Q to be $Q > 0$. This fact can make the adaptation algorithm (C1a), (C8) marginally stable, or cause a very slow convergence. If an estimate ψ_o of ψ is available, (C8) may be substituted by

$$\dot{\hat{U}}(t) = -\mu e R_{\psi_o} \eta(t) \tag{C10}$$

which, it can be shown, corresponds to $Q = (1/\left|G(j\omega_o)\right|) R_{\psi_o - \psi}$. For $\psi_o \approx Q > 0$, ensuring stability and faster convergence.

Because $e(t)$ is not directly measurable, in practice we use $y_m(t)$ instead of $e(t)$ in (C8) or (C10). In fact, we show that both signals produce asymptotically the same result. Consider the algorithm:

$$\hat{U} = -\mu \int_o^t y_m \eta(\tau)\, d\tau = -\mu \int_o^t y \eta(\tau)\, d\tau - -\mu \int_o^t e \eta(\tau)\, d\tau \underset{t \to \infty}{\to} \mu \int_o^t e \eta(\tau)\, d\tau \tag{C11}$$

where the last limit results from the assumption that ω_o is not in the spectrum of y and the well-known property of orthogonality of sinusoids of different frequencies.

The adaptation gain μ is somewhat arbitrary as long as it remains positive. In practice, however, it is chosen small to ensure a smooth evolution of the adapted parameters. Given the averaging effects shown in (C11), a small μ also helps to reduce the effects of noise in the measure of y_m.

The block diagram of the algorithm (C1a), (C8), with e substituted by y_m, is displayed in figure C–2.

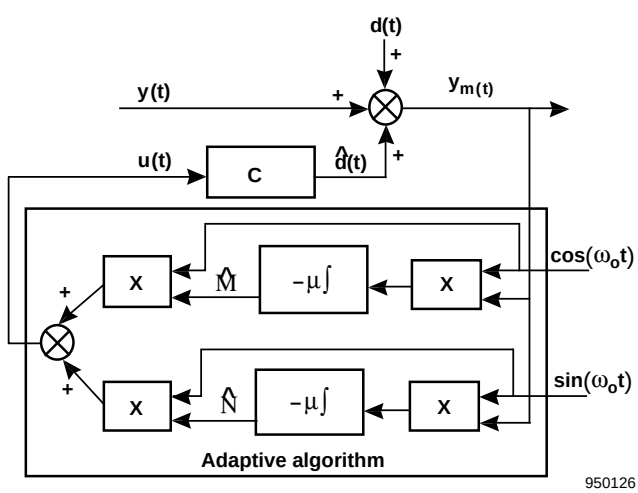

Figure C–2. Adaptive disturbance rejection algorithm.

REPORT DOCUMENTATION PAGE

Form Approved
OMB No. 0704-0188

Public reporting burden for this collection of information is estimated to average 1 hour per response, including the time for reviewing instructions, searching existing data sources, gathering and maintaining the data needed, and completing and reviewing the collection of information. Send comments regarding this burden estimate or any other aspect of this collection of information, including suggestions for reducing this burden, to Washington Headquarters Services, Directorate for Information Operations and Reports, 1215 Jefferson Davis Highway, Suite 1204, Arlington, VA 22202-4302, and to the Office of Management and Budget, Paperwork Reduction Project (0704-0188), Washington, DC 20503.

1. AGENCY USE ONLY (Leave blank)

2. REPORT DATE
March 1995

3. REPORT TYPE AND DATES COVERED
Technical Memorandum

4. TITLE AND SUBTITLE
Direct Adaptive Performance Optimization of Subsonic Transports:
A Periodic Perturbation Technique

5. FUNDING NUMBERS
WU 505-69-10

6. AUTHOR(S)
Martin España and Glenn Gilyard

7. PERFORMING ORGANIZATION NAME(S) AND ADDRESS(ES)
NASA Dryden Flight Research Center
P.O. Box 273
Edwards, California 93523-0273

8. PERFORMING ORGANIZATION REPORT NUMBER
H-2040

9. SPONSORING/MONITORING AGENCY NAME(S) AND ADDRESS(ES)
National Aeronautics and Space Administration
Washington, DC 20546-0001

10. SPONSORING/MONITORING AGENCY REPORT NUMBER
NASA TM-4676

11. SUPPLEMENTARY NOTES
Martin España is a National Research Council research associate.

12a. DISTRIBUTION/AVAILABILITY STATEMENT
Unclassified—Unlimited
Subject Category 05

12b. DISTRIBUTION CODE

13. ABSTRACT (Maximum 200 words)

Aircraft performance can be optimized at the flight condition by using available redundancy among actuators. Effective use of this potential allows improved performance beyond limits imposed by design compromises. Optimization based on nominal models does not result in the best performance of the actual aircraft at the actual flight condition. An adaptive algorithm for optimizing performance parameters, such as speed or fuel flow, in flight based exclusively on flight data is proposed. The algorithm is inherently insensitive to model inaccuracies and measurement noise and biases and can optimize several decision variables at the same time. An adaptive constraint controller integrated into the algorithm regulates the optimization constraints, such as altitude or speed, without requiring any prior knowledge of the autopilot design. The algorithm has a modular structure which allows easy incorporation (or removal) of optimization constraints or decision variables to the optimization problem. An important part of the contribution is the development of analytical tools enabling convergence analysis of the algorithm and the establishment of simple design rules. The fuel-flow minimization and velocity maximization modes of the algorithm are demonstrated on the NASA Dryden B-720 nonlinear flight simulator for the single- and multi-effector optimization cases.

14. SUBJECT TERMS
Adaptive constrained optimization; Adaptive disturbance rejection; Aircraft performance optimization; Integrated optimization; Multivariable optimization; Transport aircraft

15. NUMBER OF PAGES
42

16. PRICE CODE
AO3

17. SECURITY CLASSIFICATION OF REPORT
Unclassified

18. SECURITY CLASSIFICATION OF THIS PAGE
Unclassified

19. SECURITY CLASSIFICATION OF ABSTRACT
Unclassified

20. LIMITATION OF ABSTRACT
Unlimited